MASTER

Synthesis & characterization of two-dimensional transition metal dichalcogenide alloys: NbxW1−xS2

Lam, Cindy H.X.

Award date:
2022

Department of Applied Physics
3MA45 Graduation Project
Master thesis

Synthesis & characterization of two-dimensional transition metal dichalcogenide alloys: $\mathbf{Nb}_x\mathbf{W}_{1-x}\mathbf{S}_2$

Plasma & Materials Processing (PMP)

C.H.X. Lam

Graduation supervisors:
Ir. J.J.P.M. Schulpen
Prof. dr. A.A. Bol

Committee:
Dr. ir. H.C.M. Knoops
Dr. P. Zijlstra
Prof. dr. A.A. Bol

Eindhoven, January 2022

Abstract

The research on two-dimensional transition metal dichalcogenides (2D TMDs) has gained a lot of interest in the last few decades due to their layer-dependent properties. In contrast to their bulk counterparts, the atomically thin 2D TMD layers possess intriguing electrical, optical and catalytic properties, which makes them highly interesting for a wide variety of applications ranging from nanoelectronics to electrocatalysis. Several strategies have been proposed to further tune and improve their properties in order to expand their application domain and pave the way for industrial manufacturing. One of these methods is by alloying 2D TMDs, which enables tailoring the physical properties by varying the elemental composition. Atomic layer deposition (ALD) would be the most promising deposition technique to gain control on tuning the alloy composition. In addition, other merits provided by ALD are excellent uniformity, conformal growth across the substrate and the ability to control the film thickness at a sub-nanometer scale. The low deposition temperatures ($\leq$ 450 ºC) also make it compatible with back-end-of-line (BEOL) processes in the semiconductor industry.

In this thesis, $Nb_xW_{1-x}S_2$ alloys are synthesized using ALD, with various concentrations of x. The cycle ratio $[n{:}m]$ is used in order to control the composition by adjusting the number of n NbS_2 and m WS_2 cycles in the so-called supercycle ALD process. The characteristics of these alloys are investigated in terms of their electrical and electrocatalytic properties. Experiments show an enhancement of the electrical properties upon tuning the cycle ratio. Starting at a cycle ratio of [1:50], the resistivity ρ was found to be 5×10^5 µΩ cm. The resistivity decreases by three orders of magnitude to a value of 8.7×10^2 µΩ cm for a cycle ratio of [4:1]. This change can be related to an improvement in the conductivity due to Nb atoms acting as a p-type dopant within the WS_2 films, increasing the carrier density. In addition, results showed that pure NbS_2 is susceptible to oxidation which leads to the formation of Nb_2O_5 at the surface. The presence of Nb_2O_5 causes a slight degradation in the electrical performance of NbS_2. As WS_2 seems to be unaffected by surface oxidation, the creation of a $Nb_xW_{1-x}S_2$ alloy seems to suppress the formation of this oxide layer. The investigation on the electrocatalytic properties shows that the $Nb_xW_{1-x}S_2$ films exhibit better catalytic activity in comparison to WS_2 and NbS_2, which is attributed to the low resistivity of the alloys.

Furthermore, a novel ALD process is developed to achieve low concentrations of x with improved distribution of the dopant. The n NbS_2 cycles are replaced with n $(Nb{+}W)S_2$ cycles to obtain Nb-doped WS_2 films. In comparison to the supercycle ALD process, the resistivity is observed to decrease by a factor of two due to a better distribution of the Nb atoms within the film. Based on all the findings, it is demonstrated that ALD can be used to deposit $Nb_xW_{1-x}S_2$ films with interesting electrical and catalytic properties in contrast to NbS_2 and WS_2.

Table of Contents

Chapter 1

Introduction

As the semiconductor industry grows ever more rapidly, the quest to find new materials for applications in electronics and optoelectronic technologies is still ongoing. According to Moore's law defined in 1965, the number of transistors in integrated circuits (IC) will double every two years.[1] Since then, continuing to pursue Moore's prediction has led to a significant downscaling of the current silicon-based transistors. Where the very first semiconductor manufacturing process started at a technology node of 10 μm in 1971, progressive steps towards the nanometer scale have been made as chips with a technology node of 5 nm are now in production.

In addition to downscaling, the reduction in the sizes of the transistors has led to a transformation in their designs as illustrated in Figure 1.1. The transition from planar field-effect transistors (FETs) to vertical FET structures was realized in order to preserve their efficiency and performance. In spite of that, the advancement towards scales below the 5 nm node is starting to reach the physical limit for these transistors, as quantum tunneling effects become inevitable. These quantum effects will lead to electrons passing through barriers, which means that the current through the transistor will become difficult to control. As a consequence, the performance of the device will start to suffer from this phenomenon.[2–4] A promising circumvention of this physical limit involves the search of novel materials that could serve as an alternative for the future generation of electronic devices.
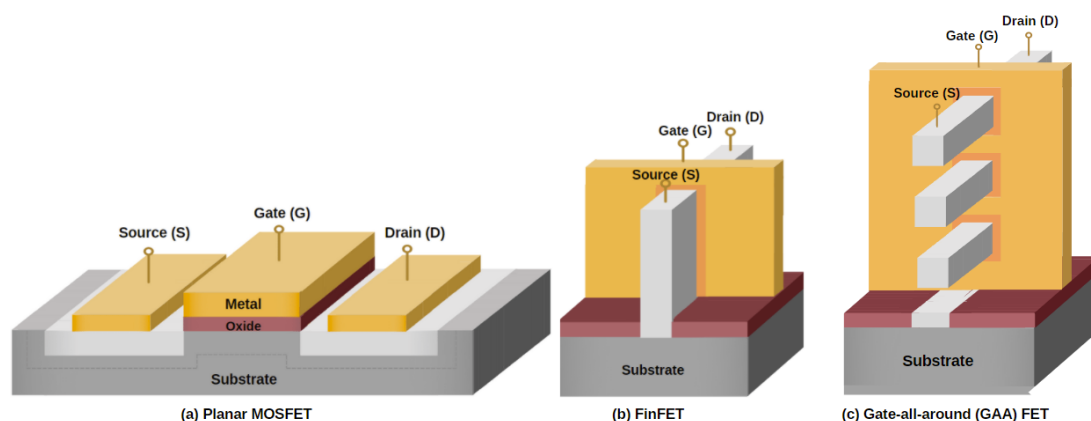
Figure 1.1: *Different architectures of field-effect transistors (FETs) based on silicon throughout the last decades. (a) The planar metal-oxide-semiconductor FET (MOSFET) was first introduced in 1960 and is the most common semiconductor device used in ICs. (b) The FinFET architecture with vertical structures is introduced in the industry in 2010 for the processes around the 20-nm scale. (c) The gate-all-around (GAA) FET is the design for the transistors below the 5-nm scale.*

In the last few years, two-dimensional (2D) materials are considered to be one of the trending materials to investigate due to their fascinating properties. The discovery and characterization of graphene back in 2004 by Andre Geim and Konstantin Novoselov showed excellent properties in terms of electrical and thermal conductivity at a single atomic layer thickness, which has led to the Nobel Prize in Physics in 2010.[5] This observation of outstanding properties of such atomically thin layers sparked the interest of the scientific community to explore and develop other 2D materials. Since then, a large number of other 2D materials have been synthesized, including hexagonal boron nitride (h-BN), silicene (2D silicon), germanene (2D germanium), transition metal di- and trichalcogenides (2D TMDs/TMTs), MXenes, and many more.[6,7] The 2D TMD class is particularly of great interest due to their versatile properties, different from graphene. They show a wide spectrum of characteristics, ranging from insulators to semiconductors and even (semi)metals, making them diversely applicable.

1.1 Transition metal dichalcogenides (TMDs)

The atomic composition of 2D TMDs is defined by the general formula MX_2, where M is the transition metal atom given in the periodic table by groups 4-10 and X is the chalcogen atom (S, Se, or Te). The structure of a TMD material is illustrated in Figure 1.2. A bulk TMD material is composed of atomically thin layers that are weakly bonded by van der Waals forces, also known as the 'van der Waals gap'. Each layer consists of one atomic layer of the transition metal atom that is sandwiched between two monolayers of chalcogen atoms, connected by in-plane covalent bonds. Depending on the orientation of the chalcogen atoms and their layered stacking order, the 2D TMDs can exhibit various different structural phases, which will be further elaborated in Chapter 2.
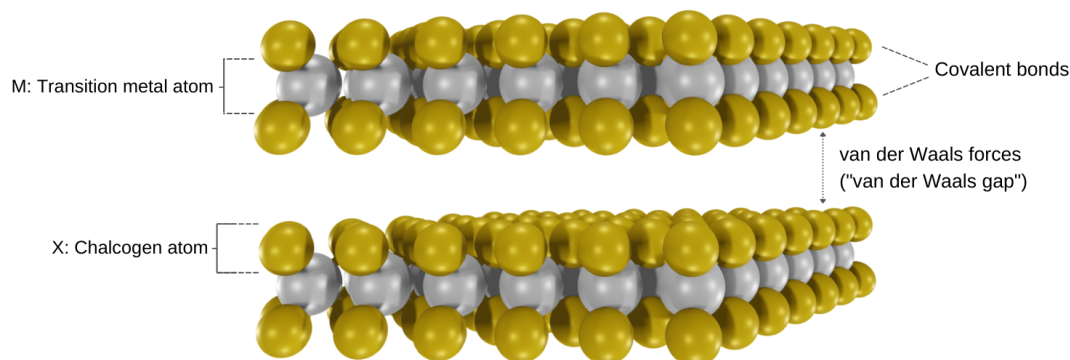
Figure 1.2: *Structure of the transition metal dichalcogenides (TMDs), where the chalcogen atoms (yellow) and metal atoms (gray) are bound together by covalent bonds. The layers are held together by van der Waals forces.*

The relative weakness of the van der Waals interactions between the layers allow for the isolation of single nanosheets that exhibit unique properties that are different from their 3D bulk counterparts due to quantum confinement and broken inversion symmetry.[7,8] Consequently, the conversion from bulk to a monolayer for several semiconducting TMDs like molybdenum disulfide (MoS_2) and tungsten disulfide (WS_2) leads to the transition from an indirect to direct bandgap in the electronic bandstructure. This is relevant since a direct bandgap strongly enhances the photoluminescence emission, which is essential for optoelectronic devices such as solar cells and light-emitting diodes (LEDs). Additionally, TMDs are highly attractive as biosensors[9,10] and catalysts[11,12] due to their large surface-to-volume ratio. An overview of potential applications of TMDs can be seen Figure 1.3. While individual 2D TMDs already demonstrate properties that can be used for practical applications, combining TMDs to form ternary or quaternary compounds could even further optimize their performance. Therefore, the ability to generate novel and improved properties can expand their field of application to meet the requirements for future technologies.
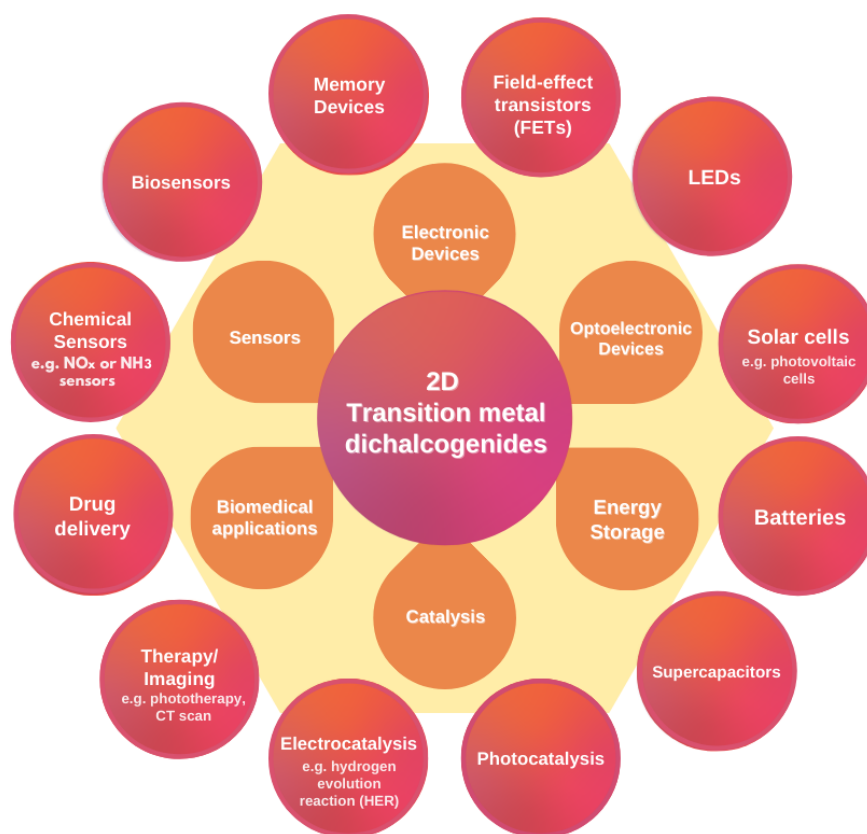
Figure 1.3: *An overview of the wide range of applications of 2D TMDs.*

1.2   Alloying TMDs: Tuning the properties

Several strategies have been proposed to tune the properties of 2D TMDs to increase their potential for practical device applications even further. Alloying would be one of these strategies, which involves mixing an additional element into the transition metal or the chalcogen sublattice to form 2D TMD structures consisting of three elements. The general formula to represent a ternary TMD structure where an additional transition metal is introduced is $M'_xM''_{1-x}X_2$, with M' and M" being two different transition metals and x is a number between 0 and 1. Alternatively, the structure for a TMD containing two chalcogen types is given by $MX'_{2x}X''_{2(x-1)}$, where X' and X" are two different chalcogens.[13]
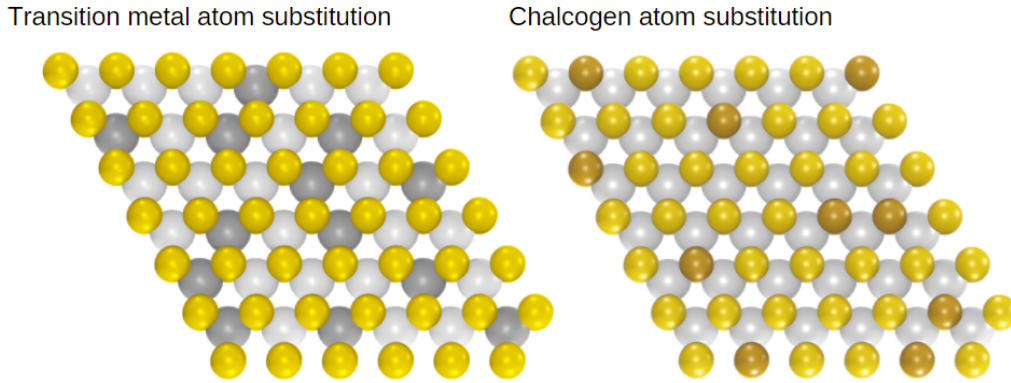
Figure 1.4: *Representation of the structure resulting from the subsitution of a transition metal atom ($MX'_{2x}X''_{2(x-1)}$ alloys) or a chalcogen atom ($MX'_{2x}X''_{2(x-1)}$ alloys) in the respective sublattices of the 2D TMD*

The intermixing of 2D TMD materials from different groups in the periodic table has not yet been studied extensively in the research community, while this could lead to the discovery of intriguing materials. WS_2 is of interest for the use in electronic devices as a conductive channel between the source and drain electrodes. However, its performance is still lacking compared to the materials that are conventionally used in transistors nowadays. On the other hand, the metallic nature of niobium disulfide (NbS_2) shows excellent performance in terms of electrical conductivity. Earlier reported studies presented improvements in the electrical transport by combining WS_2 and NbS_2 to form a $Nb_xW_{1-x}S_2$ alloy.[12,14,15] Besides, the combination of these two materials could be beneficial for electrocatalytic water splitting. For WS_2 nanosheets, the catalytically active sites are only present at the edges of the sheets, while the surface of the material remains inert. The presence of an inert surface is however not the case for NbS_2, where the surface is also chemically active.[11,12] The chemically reactive sites of metallic TMDs and their relatively high electrical conductivity makes it possible to enhance the catalytic performance of semiconducting TMDs like WS_2.

1.3 Atomic layer deposition (ALD)

The search for new materials for the applications seen in Figure 1.3 hinges on the deposition technique to achieve these thin-film structures. A method proposed to synthesize 2D TMD alloys is by atomic layer deposition (ALD). ALD is a gas-phase deposition technique that depends on self-limiting surface reactions in order to grow the film onto the substrate. The general ALD process consists of two half-cycles, each comprising of two steps: a precursor/co-reactant step followed by a purging step. A schematic overview of the ALD cycle can be seen in Figure 1.5.
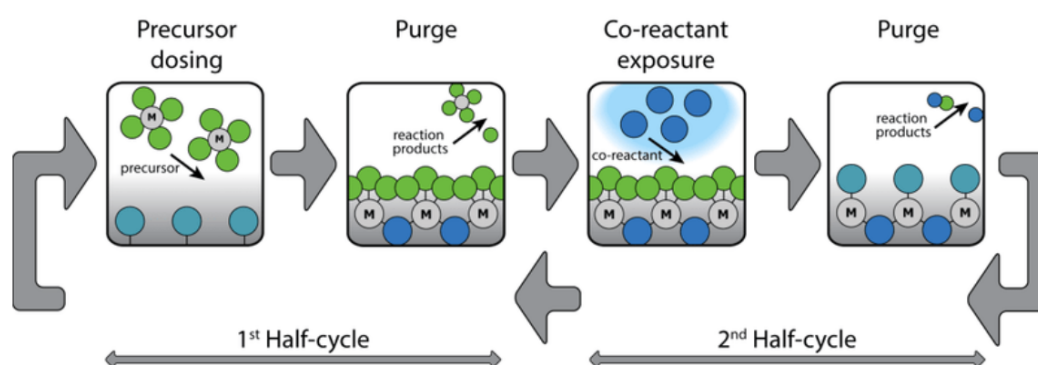
Figure 1.5: *Schematic illustration of the two half-cycles that make up the ALD cycle. The first half-cycle introduces the precursor molecules to the substrate surface. In the second half-cycle, the surface is exposed to the co-reactant in order to build the film. Each dosing step is followed by a purging step.*[16]

In the first half-cycle, the surface of the substrate is exposed to the precursor molecules. As the precursor molecules do not react with each other, saturation is reached when no more adsorption sites are available on the surface. Subsequently, the remaining precursor molecules and reaction by-products are removed by a purging step with an inert gas (e.g. Ar) in order to prevent parasitic chemical vapor deposition (CVD) processes to take place. In the second half-cycle, the co-reactant is introduced, which reacts with the adsorbed precursor molecules. The co-reactant replaces the ligands of the precursor molecules with reactive groups to form the first layer and subsequently, a purging step is performed again to remove the reaction by-products. This cycle is repeated until the desired thickness is achieved. The surface reactions may be driven by thermal energies or by a plasma source during the co-reactant step. The former is known as thermal ALD, while the addition of a plasma during the co-reactant step that introduces radicals, ions and UV radiation is known as plasma-enhanced ALD (PE-ALD).

The main advantages of ALD due to its self-limiting nature are the excellent uniformity and conformality it provides across the substrate and the ability to control the film thickness at an Ångström (Å) level by controlling the number of ALD cycles.[17] Moreover, the ability to deposit thin films at low temperatures ($\leq$ 450 ºC) makes ALD compatible for use in industrial semiconductor manufacturing processes.

1.4   Research questions and outline

Several studies have reported the fabrication of $Nb_xW_{1-x}S_2$ alloys by CVD[12,14,18] at high temperatures (800 - 830 ^oC). Nonetheless, literature employing other deposition techniques to obtain these alloys seems rather absent. In order to define the characteristics of $Nb_xW_{1-x}S_2$, the development of a novel PE-ALD process is considered by combining the individual binary ALD processes of NbS_2 and WS_2.[19,20] The properties of these alloys as a function of their composition are investigated with the main focus on the electrical aspects and their electrocatalytic activity. The main research questions at the beginning of this project are:

1. Can we accurately control the $Nb_xW_{1-x}S_2$ alloy composition using advanced ALD deposition schemes?

2. Can we improve the catalytic activity of WS_2 and NbS_2 by synthesizing a $Nb_xW_{1-x}S_2$ alloy?

3. Can we achieve a 2D TMD alloy with electrical properties suitable for the implementation in FETs?

Chapter 2 provides the basic understanding of the structure and properties of TMDs. Additionally, a literature review on earlier reported studies of $Nb_xW_{1-x}S_2$ alloys is also given. In Chapter 3, the experimental details of the synthesis and characterization set-ups are described, including the design of the ALD process for the $Nb_xW_{1-x}S_2$ alloys that is inspired from previous works of the WS_2 and NbS_2 processes within the group. A series of samples is made with controlled compositions ranging from W-rich to Nb-rich. The results for the ALD grown $Nb_xW_{1-x}S_2$ films are reported and discussed in Chapter 4. Here, the growth characteristics, compositional changes and the electrical properties have been investigated. Furthermore, an additional third step (ABC process) is developed to incorporate in the ALD process with the aim to obtain low values of x with an improved dopant distribution. In Chapter 5, the electrocatalytic properties of the $Nb_xW_{1-x}S_2$ films are studied by measuring the electrochemical properties to evaluate their potential as an electrocatalyst for the hydrogen evolution reaction (HER). An overview of the findings and a conclusion are given in Chapter 6, providing answers to the first two research questions that have been defined at the initial stage of this thesis. Finally, a follow-up research of the third research question is considered in Chapter 7, as well as additional experiments that can be conducted for these alloys.

Chapter 2

Structure and Properties of Transition Metal Dichalcogenides

This chapter provides the basic understanding of TMD materials in terms of their structural, electronic and electrical properties. In Section 2.1, a brief explanation on the crystal structure of TMD materials is presented. The distinct material properties of WS_2 and NbS_2 can be explained by the differences in their electronic bandstructure, where WS_2 shows semiconducting behavior and NbS_2 is metallic. In addition, a literature review on $Nb_xW_{1-x}S_2$ considers the compatibility of mixing WS_2 and NbS_2 in comparison to other group 5 transition metals. Density functional theory (DFT) calculations from studies examined different configurations for the substitution of the Nb atoms within the WS_2 lattice structure, showing the most energetically favorable structure for the alloys. This leads to changes in the electronic bandstructure of the material. In Section 2.2, the vibrational modes of the crystal structure are discussed, which can be used to characterize the composition and crystallinity of the material through Raman spectroscopy. The electrical properties like the carrier mobility, conductivity and the resistivity are described in Section 2.3, including the effects of temperature and scattering mechanisms on the carrier mobility and resistivity of the material.

2.1   Crystal and electronic structure

The 2D TMD structure comprises of three atomic sublayers in a hexagonally close-packed (hcp) structure, which was shown in Figure 1.2. Each transition metal atom is bonded to six chalcogen atoms of which three are located at the top and three at the bottom sublayer. The thickness of a TMD layer including the interlayer spacing ranges between 6 and 7 Å, depending on the size of the constituent elements and the bond length that defines the average distance between the nuclei of two bonded atoms. Since the layers that make up a bulk TMD crystal are held together by weak van der Waals forces, single layers of the material can be isolated by e.g. mechanical exfoliation.[8]

The presence of the three atomic sublayers gives rise to various arrangements that the atoms can adopt, leading to two types of structural phases for the TMD crystals, which are depicted in Figure 2.1. The first type is the 2H phase, which has the trigonal prismatic coordination and a hexagonal (H) symmetry. The unit cell consists of two X-M-X units containing six atoms in total. The second type is the 1T phase that has an octahedral coordination with tetragonal (T) symmetry and consists of one X-M-X unit per unit cell. For the bulk crystal, there is also the 3R phase with rhombohedral (R) symmetry, which has an identical trigonal prismatic coordination like the 2H phase. However, the 3R phase consists of three X-M-X units per unit cell, so it possesses a different stacking order.
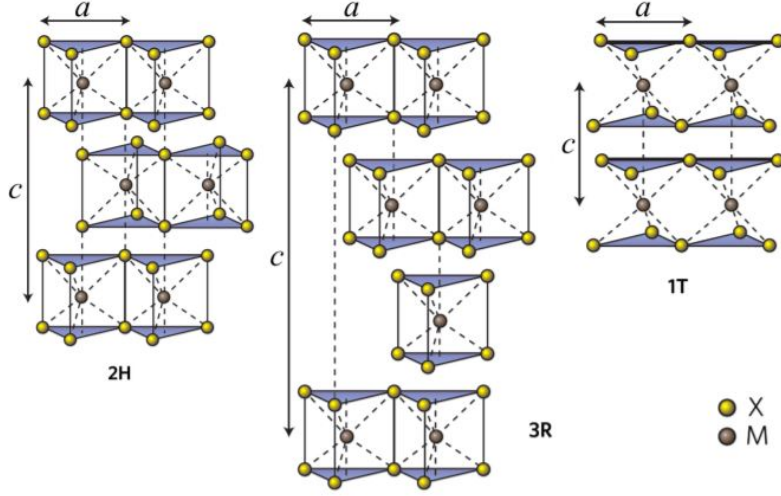
Figure 2.1: *The different structural phases of TMD layers: 2H, 3R and 1T phases. Here, a is the axis along the plane (in-plane) and the minimal distance between two metal or two chalcogen atoms, and c, the axis perpendicular to the layers (out-of-plane).*[21]

The coordination geometry of TMDs and the number of d electrons of the transition metal atoms are essential in determining the electronic structure of TMDs. If the highest orbital is partially filled (odd numbers of electrons), the material will show metallic characteristics. On the other hand, if the highest orbital is fully occupied (even number of electrons), the material is a semiconductor. Although the band structure is formed by the hybridization between the p orbitals (p_x, p_y, p_z) of the chalcogen atoms and the d orbitals ($d_{z^2}, d_{x^2-y^2}, d_{xy}, d_{yz}, d_{xz}$) of the transition metal atoms, the electronic properties are mostly dominated by the transition metal atoms.[1]

2.1.1 Literature review on $Nb_xW_{1-x}S_2$

A theoretical analysis of the band structure of $Nb_xW_{1-x}S_2$ can be performed using first-principle density functional theory (DFT) calculations. The studies on the electronic structure could provide the underlying nature of the material properties to substantiate the experimental results. The band structures of WS_2 and NbS_2 for the bulk and single TMD layer can be observed in Figure 2.2.

The crystal structure of WS_2 often occurs in the form of the 2H phase, as it is the most energetically favorable structure. WS_2 is a semiconducting TMD material, demonstrating a layer-dependent band structure as seen in Figure 2.2. The transition from an indirect to a direct bandgap upon decreasing the number of layers arises from the absence of the interlayer coupling between neighboring layers.[22] On the other hand, NbS_2 can occur either in the 2H or 3R phase. It exhibits metallic characteristics due to an odd number of valence electrons, thereby not having a bandgap as the Fermi level resides within the conduction band. The metallic characteristics lead to NbS_2 having a very high electrical conductivity, which makes it suitable for electronic devices to use it as a contact electrode.[10]
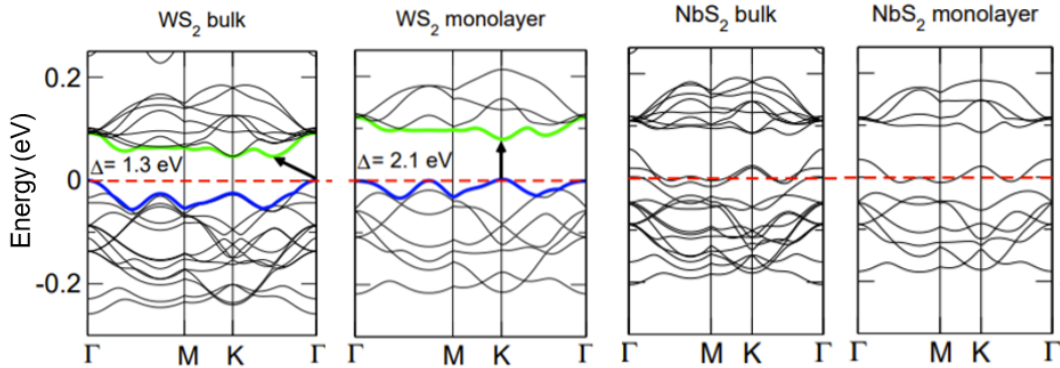
Figure 2.2: *The bandstructure of 2H-WS$_2$ and 3R-NbS$_2$ obtained from DFT calculations on a bulk material and monolayer. The red dashed line indicates the Fermi level. For WS$_2$, the arrows indicate the indirect (WS$_2$ bulk) and direct (WS$_2$ monolayer) bandgap with the smallest value. The conduction band minimum is indicated by green, while the valence band maximum is highlighted in blue. Adapted from[23]*

The lattice parameters and the calculated bandgaps of WS$_2$ and NbS$_2$ are presented in Table 2.1. The results show that they have slightly different lattice constants, corresponding to a lattice mismatch of approximately 4.5%. This is slightly larger than the value of 3.4%, which is the maximum mismatch allowed between two TMDs as suggested by Kutana *et al.*[24] to form an alloy.

Table 2.1: The lattice parameters and electronic bandgap of WS$_2$ and NbS$_2$[23,25]

TMD Material	a (Å)	c (Å)	M-X Bond length (Å)	Bandgap (calc.,eV)
WS$_2$	3.16	12.32	2.40	1.3-1.8
NbS$_2$	3.31	11.97	2.42	0

Additionally, recent studies on the electronic band properties of Nb$_x$W$_{1-x}$S$_2$ alloys have been performed based on DFT calculations to gain insight on structural changes at low concentrations x. Li *et al.*[26] performed a computational study on the structural and electronic properties of p-type doped WS$_2$ monolayers by several transition metals including Nb. The analysis on the stability of these doped structures was determined by the formation energy E_{for}, which is obtained from DFT calculations. Substitutional doping of Nb in WS$_2$ monolayers showed the lowest formation energy ($E_{for} = -2.305$ eV), indicating that it is the most energetically favorable structure in comparison with the other group 5 metals (V and Ta).

Jin *et al.*[14] considered several possible configurations for the substitution of Nb atoms into the lattice structure of WS$_2$, which can be seen in Figure 2.3 The formation energies were calculated using DFT calculations. Four kinds of doped structures were considered: (i) substitutional doping of Nb at the W site, (ii) substitutional doping of Nb at the S site,

(iii) a Nb adatom above the W atom, and (iv) Nb adatom above the S atom. The most energetically favorable configuration was found for substitutional doping of Nb at the W site. This shows that Nb dopants will have a preference to be incorporated in the sublayer of the W atoms, rather than in the sublayer of the S atoms or intercalated between the layers. This is also supported by a study of Gao *et al.*,[27] where it was observed that Nb atoms indeed replaced W atoms in the transition metal sublattice. It was shown that the addition of Nb in the WS_2 layers displayed a shift in the Fermi level towards the valence band maximum (VBM) due to having one electron less in comparison with W giving rise to *p*-type characteristics.
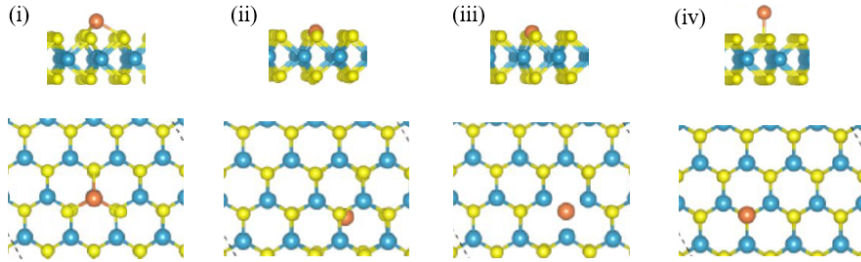
Figure 2.3: *The four different Nb-doping configurations: (i) substitutional doping of Nb at the W site, (ii) substitutional doping of Nb at the S site, (iii) Nb adatom above the W atom, (iv) Nb adatom above the S atom. Adapted from*[14]

2.2 Vibrational modes

The unit cell for the 2H phase of both TMDs consists of six atoms, which give rise to 18 vibrational modes that can be decomposed into the irreducible representation at the center of the Brillouin zone Γ:

$$\Gamma = A_{1g} + 2A_{2u} + 2B_{2g} + B_{1u} + E_{1g} + 2E_{1u} + 2E_{2g} + E_{2u}. \tag{2.1}$$

The A_{1g}, E_{1g} and E_{2g} are first-order Raman active modes, while A_{2u} and E_{1u} are infrared (IR) active. The B_{2g}, B_{1u} and E_{2u} modes are optically silent and therefore cannot be detected by Raman or IR spectroscopy.[28,29]

For the 3R phase, the irreducible representation of the Brillouin zone is given by[30]

$$\Gamma = 3A_1 + 3E, \tag{2.2}$$

where two A_1 and two E are Raman active modes. A schematic illustration of the vibrational modes is illustrated in Figure 2.4. The A_{1g} mode involves the motion of the chalcogen atoms along the *c*-axis, moving perpendicular to the layers and therefore out-of-plane. The E_{1g} mode represents the motion of the chalcogen atoms along the *a*-axis. The E_{2g} mode is the vibrational mode that involves the motion of both the transition metal and chalcogen atoms in-plane along the *a*-axis. Second-order Raman scattering can be

observed if resonant excitation occurs. This type of scattering is enhanced by the coupling of phonon modes to electronic states that are optically excited in the crystal. At an excitation wavelength of 514.5 nm, second-order Raman modes such as the longitudinal acoustic (LA(M) and 2LA(M)) modes can be observed for WS_2.[31] The Raman modes allow for the characterization of a TMD material, the number of TMD layers that are present, and the crystallinity of the material, which will be further discussed in Chapter 3.
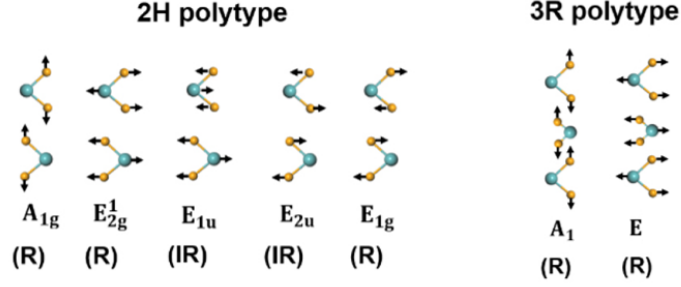
Figure 2.4: *The vibrational modes of the transition metal atoms (blue) and chalcogen atoms (yellow). The Raman active modes are: E_{2g}, E_{1g} and A_{1g} modes for the 2H and 3R phase, where the E_{2g} mode is doubly-degenerate. Adapted from[32]*

2.3 Electrical transport properties

The electrical properties of TMD materials are defined by the transport and scattering of the charge carriers. When an external electric field $\vec{E}$ is applied to a material, the carriers respond by moving with an average velocity known as the drift velocity $\vec{v}_D$. If the density of charge carriers n is known, then the current density $\vec{J}$ is defined as follows by Ohm's law,

$$\vec{J} = ne\vec{v}_D = \sigma\vec{E}, \tag{2.3}$$

where q is the elementary charge. The conductivity σ of a material is the constant relating the current density and the external electric field. The constant of proportionality in the linear relation between the electric field and drift velocity is given by by the carrier mobility μ,

$$\vec{v}_D = \mu\vec{E}, \tag{2.4}$$

where

$$\mu = \frac{e\tau}{m_{\text{eff}}}. \tag{2.5}$$

The carrier mobility of a material defines the motion of a charge carrier (electron or hole) under influence of an external electric field. Here, τ is the scattering time and m_{eff} is the

effective carrier mass. The mobility is inversely proportional to the effective mass of the carrier, which indicates that a low effective mass results in a higher mobility, and vice versa. The mobility also depends on the scattering time, which is the average time in-between subsequent collisions of the carriers with phonons and impurities in the lattice.

For a metal, the conductivity σ is given by the electron density n_e, the elementary charge, the scattering time and the effective mass,

$$\sigma = ne\mu = \frac{n_e e^2 \tau}{m_{\text{eff}}}. \tag{2.6}$$

For a semiconductor, the conductivity is given by the electrons n_e and holes n_h and their respective mobility μ_e and μ_h given by[33]

$$\sigma = e(n_e \mu_e + n_h \mu_h). \tag{2.7}$$

By doping semiconductors, the conductivity can be modified due to the introduction of impurities in the crystal lattice. The addition of impurities leads to extrinsic semiconductors and therefore an increase in the carrier density. A relation between the conductivity and the resistivity of the material can also be defined. The resistivity ρ is defined as the reciprocal of the conductivity given by

$$\rho = \frac{1}{\sigma}. \tag{2.8}$$

2.3.1 Scattering mechanisms

The mobility of carriers can be affected by several scattering mechanisms: optical and acoustic phonon scattering, ionized impurity scattering, and scattering by defects. Thin-film materials like 2D TMDs become prone to structural disorders like grain boundaries and point defects. As a consequence, grain boundary scattering and surface scattering are more dominant.[34]

The formation of an alloy results in random positioning of substituted atoms in the crystal lattice. This alteration in composition may lead to perturbations in the crystal potential, thereby acting as scattering centers. This leads to another scattering contribution that needs to be taken into account. All these processes could decrease the scattering time of the carriers, increasing the overall resistivity ρ of the material. The contribution of all these scattering mechanisms can be determined using Matthiessen's rule, which states that the scattering rate is given by the sum of all the inverse scattering times of the various mechanisms,

$$\frac{1}{\tau} = \sum_i \frac{1}{\tau_i}. \tag{2.9}$$

where τ_i is the scattering time belonging to scattering mechanism i. This shows that all the different scattering mechanisms are independent of one another. Analogous to Equation 2.9, we can write the mobility as

$$\frac{1}{\mu} = \sum_i \frac{1}{\mu_i}.$$
(2.10)

2.3.2 Temperature-dependence of the resistivity

When the temperature changes, then this will influence the scattering mechanisms and hence the resistivity of a material.[35] The temperature dependence of the resistivity can be approximated by

$$\rho = \rho_0(1 + \alpha_0 \Delta T),$$
(2.11)

where ρ_0 is the resistivity at room temperature, α_0 is the temperature coefficient of the resistivity at room temperature, and $\Delta T = (T - T_0)$, the difference between the temperature and room temperature T_0.

The resistivity shows a different temperature-dependence depending on whether the material is a metal or a semiconductor. For a metal, an increase in the temperature leads to additional thermal energy that causes an enhancement in the atomic vibrations within the lattice structure. The thermal vibrations increase the scattering cross-sections of the atoms for which the carriers will interact during their movement, resulting in a decrease in the scattering time and thereby an increase in the resistivity ($\alpha_0 > 0$).

For a semiconductor, higher temperatures provide the energy for electrons to cross the band gap and move from the valence to the conduction band. This leads to an increase in the carrier concentration and more carriers that contribute to the conductivity of the material, hence a decrease in the resistivity ($\alpha_0 < 0$). The mobility is also be affected by the temperature change due to different scattering mechanisms that are dominant for certain temperature ranges. At low temperatures, ionized impurity scattering ($\mu \propto T^{3/2}$) will be more important. At higher temperatures, phonon scattering ($\mu \propto T^{-3/2}$) is considered to be the dominant factor.[36]

Chapter 3

Experimental Details and Characterization Principles

This chapter provides an overview of the synthesis and characterization techniques that are used for this research. In Section 3.1, the set-up and recipe of the ALD process on forming the $Nb_xW_{1-x}S_2$ are discussed. In order to create the alloy, a supercycle process is employed where we alternate between WS_2 and NbS_2 ALD cycles. In Section 3.2, details on the optical characterization techniques such as spectroscopic ellipsometry (SE) and Raman spectroscopy are given. These techniques are used to define the film growth and crystallinity of the $Nb_xW_{1-x}S_2$ alloys, respectively. This is also followed by x-ray photoelectron spectroscopy (XPS), which is used to determine the chemical composition of the material. To obtain further insight on the morphology of the material, electron microscopy imaging techniques such as scanning electron microscopy (SEM) and transmission electron microscopy (TEM) are used and presented in Section 3.3. Electrical characterization techniques such as four-point probe (FPP) and the Hall effect are used to examine the electrical properties of the alloys for different values of x, which are described in Section 3.4.

3.1 Atomic layer deposition (ALD)

The thin films were prepared using a PE-ALD process in a FlexAL ALD reactor of Oxford Instruments, a schematic illustration of this set-up is depicted in Figure 3.1. The main components of the reactor are the load lock, the reaction chamber, and the remote inductively coupled plasma (ICP) source operating at a frequency of 13.56 MHz for generating the plasma. In addition, the precursors used for the process are contained in stainless steel cylindrical bubblers that are attached to the reactor.

To start with the ALD process, a wafer is placed into the load lock, which is equipped with a pump to bring the pressure down to vacuum levels. After that, the wafer is transferred to the reaction chamber. The reaction chamber is kept at a base pressure of $\sim 10^{-6}$ mTorr. The wafer is then placed on a table with a substrate heater that controls the table temperature. Within the research group, processes for WS_2 and NbS_2 had already been realized by Balasubramanyam[20] and Basuvalingam[19] respectively. Based on their works for WS_2 and NbS_2, a novel ALD process for the synthesis of $Nb_xW_{1-x}S_2$ was developed for this research.

The first half-cycle of either the WS_2 or NbS_2 ALD process starts with one of the metal-organic precursors that is sent to the chamber, using Ar as a carrier gas. The metal-organic precursors bis(tert-butylimino)bis(dimethylamino)tungsten (BTBMW) and tris(diethylamido)(tert-butylimido) niobium (TBTDEN) are used for the deposition of W and Nb atoms respectively. The chemical structure of these two precursors is also presen-

ted in Figure 3.1. The dose time for both precursors is set to 10 s to ensure saturation at the substrate surface.[19,20] In the second half-cycle, a mixture of a H_2S plasma and Ar gas (10:40 sccm) is used with a dosing time of 30 s. An ICP source with a power of 200 W generated the H_2S plasma gas mixture. The precursor dosing and the co-reactant step are separated by an Ar purging step using a mass flow rate of 300 sccm for a duration of 10 s. The table temperature is fixed at 450 °C and the walls of the reactor are kept at 150 °C during all the processing steps.
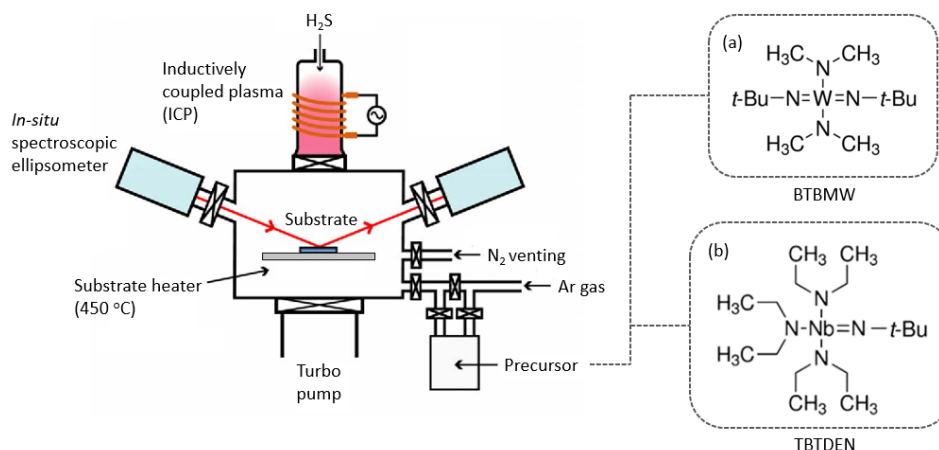
Figure 3.1: *Schematic illustration of the FlexAL ALD reactor and the chemical structures of the used precursors; (a) Bis(tert-butylimino)bis(dimethylamino)tungsten (BTBMW) and (b) Tris(diethylamido)(tert-butylimido)niobium (TBTDEN). Adapted from*[37]

3.1.1 Supercycle process

The $Nb_xW_{1-x}S_2$ alloys are created by combining the individual binary PE-ALD processes of WS_2 and NbS_2. The approach that is used to synthesize a ternary material using ALD involves the supercycle process, where a number of WS_2 and NbS_2 cycles are performed subsequently after one another. Here, the number of cycles for WS_2 and NbS_2 can be controlled independently of each other. A schematic illustration of this is shown in Figure 3.2, where the ALD process of WS_2 consists of m cycles and NbS_2 of n cycles. The composition of the alloy can be tuned by controlling two parameters of the supercycle process, namely the cycle ratio and the supercycle length.

First, the cycle ratio between Nb and W [$n{:}m$] can be varied in order to obtain different values for x. Secondly, the total number of ALD cycles in the supercycle is given by the supercycle length, equivalent to $n + m$. The supercycle length is the second important parameter which allows for the control of the mixing of the elements in the composition. Large supercycle lengths yield the deposition of distinct layers of the individual materials, resulting in a multilayered film. In contrast, shorter supercycle lengths lead to intermixing between the two constituent transition metals to form a well-mixed film.

Figure 3.2: *Schematic overview of the supercycle PE-ALD process for the $Nb_xW_{1-x}S_2$ alloy, using the precursors BTBMW and TBTDEN for W and Nb respectively, and H_2S as the co-reactant for the deposition of S atoms.*

The film composition and the growth of the alloys for different cycle ratios can be described by the rule of mixtures, given by Equations 3.1 and 3.2,[38]
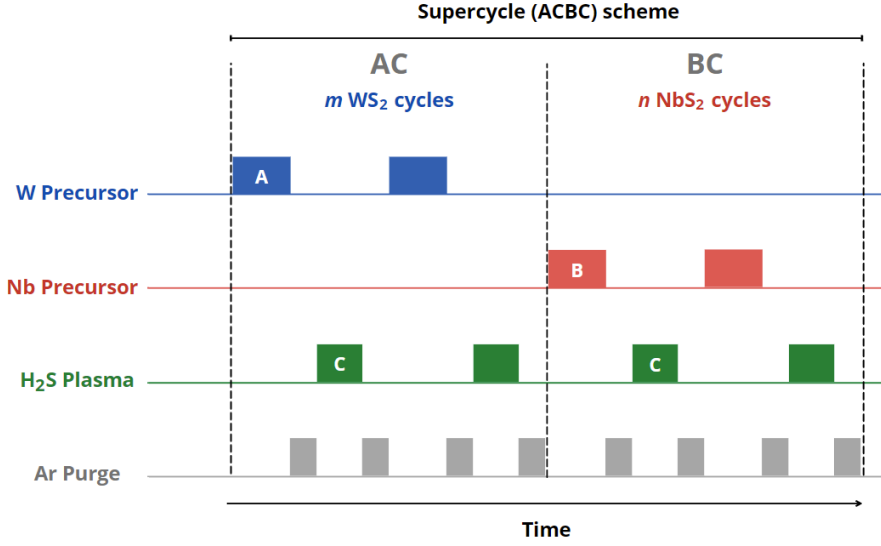
$$\text{GPC}_{\text{alloy}} = \frac{n}{n+m} \times \text{GPC}_{\text{NbS}_2} + \frac{m}{n+m} \times \text{GPC}_{\text{WS}_2}, \qquad (3.1)$$

where $\text{GPC}_{\text{alloy}}$, $\text{GPC}_{\text{NbS}_2}$ and GPC_{WS_2} are in Å. According to Equation 3.1, the film growth of the alloy should be a linear combination of the individual growth per cycle (GPC) of WS_2 and NbS_2, weighted by the cycle fractions. In practice, the growth rate of the alloy can deviate from the expected linear growth. This could be due to the presence of a nucleation delay when switching the individual binary cycles, leading to a lower growth rate in comparison with the theoretical prediction. Another possibility is an increase in the number of active sites on the surface due to changes in the morphology when depositing two different materials. The relatively large number of active sites will therefore lead to a higher growth rate than expected. The atomic film composition of the alloy is defined by the following equation:

$$x = \frac{[\text{Nb}]}{[\text{Nb}] + [\text{W}]} = \frac{\frac{n}{n+m} \times \text{GPC}_{\text{At,NbS}_2}}{\frac{n}{n+m} \times \text{GPC}_{\text{At,NbS}_2} + \frac{m}{n+m} \times \text{GPC}_{\text{At,WS}_2}}, \qquad (3.2)$$

where [Nb] and [W] are defined as the concentrations of Nb and W respectively. The composition x depends on the atomic growth rates (GPC_{At}) and the cycle fractions of the individual binary materials. The atomic growth rates are defined as the number of atoms that are deposited per WS_2 or NbS_2 cycle.

3.2 Composition and optical characterization techniques

3.2.1 Spectroscopic ellipsometry

The thickness and the optical properties of thin-film materials can be characterized by spectroscopic ellipsometry (SE). In this experimental technique, a light beam with a known polarization state is used to probe the interaction of the light and the sample. As a result of this interaction, the polarization state of the reflected light beam that is detected by the ellipsometer will be different. This is schematically depicted in Figure 3.3.
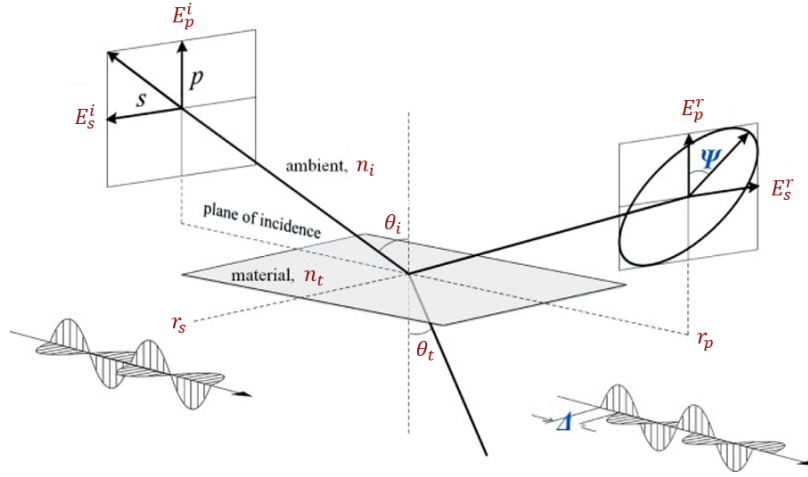
Figure 3.3: *Schematic representation of the change in the polarization state of light upon reflection from the surface of a sample. Adapted from*[39]

The changes in the polarization state can be described by the Fresnel equations. These equations define the change in the reflected and transmitted electric field components of the incident light upon reaching an interface that separates two different media. In case of a single interface, the reflection coefficients for perpendicularly polarized light (r_s) and light with a polarization parallel to the plance of incidence (r_p) are given by the complex refractive indices $n_{i,t}$ and the angles of incidence $\theta_{i,t}$:

$$r_s = \frac{n_i \cos \theta_i - n_t \cos \theta_t}{n_i \cos \theta_i + n_t \cos \theta_t} = \frac{E_s^r}{E_s^i}, \qquad r_p = \frac{n_t \cos \theta_i - n_i \cos \theta_t}{n_i \cos \theta_t + n_t \cos \theta_i} = \frac{E_p^r}{E_p^i}. \tag{3.3}$$

The ellipsometer measures the change in the ratio of the reflectance of light normal to the plane of incidence (R_s) to the reflectance of light parallel to the plane of incidence (R_p), which is given by the reflectivity ratio $\tan (\Psi)$ and the phase shift of the components Δ both as a function of the wavelength.[40] The reflectance is related to the square amplitude of the electric field components given in Equation 3.3:

$$\frac{R_p}{R_s} = \frac{|r_p|^2}{|r_s|^2} = \tan \Psi \cdot e^{i\Delta} = \rho. \tag{3.4}$$

The SE measurements were performed *in-situ* during deposition to monitor the film growth of the alloys, using a J.A. Woollam Co., Inc., M2000U with the photon energy ranging between 1.25 and 5 eV. The ellipsometric spectra were obtained after every individual binary ALD cycle of WS_2 and NbS_2. The film thickness of the alloys was determined by using CompleteEASE$^\copyright$ software to fit the data from the SE measurements by a model. In this model, the effective medium approximation (EMA) is used to define the $Nb_xW_{1-x}S_2$ layer. The calculation is based on the optical constants of WS_2 and NbS_2, which have been obtained by B-spline interpolation.

3.2.2   Raman spectroscopy

Raman spectroscopy is a widely used technique to determine the vibrational modes of molecules, often used to characterize materials and also their crystallinity. In general, it is based on the interactions that a photon from light will have with a molecule, for which it can be scattered or absorbed. A schematic illustration is shown in Figure 3.4. For Rayleigh scattering, the photon is absorbed by the molecules, only to be emitted again at the same energy and thereby the same wavelength.[41] In case the photon loses energy, its wavelength increases and this is known as a Stokes shift. Inversely, an anti-Stokes shift occurs when the photon gains energy, and thus has a smaller wavelength after interacting with the material. These Raman shifts correspond to a specific vibrational mode of the molecule and can be observed in the resulting Raman spectrum.[42]

As previously treated in Section 2.2, the modes can characterize the TMD material, as well as its crystallinity. Amorphous or crystalline solids can have a significantly different Raman spectra even though their chemical composition is equivalent. Crystalline solids consist of a crystal lattice with repeating unit cells, possessing long-range ordering. For amorphous solids, the long-range ordering is absent which results that the characteristic Raman modes cannot be distinguished. Hence, Raman spectroscopy can define the crystallinity of the material. The measurements on the $Nb_xW_{1-x}S_2$ alloys were performed using a Renishaw Invia Raman microscope with an excitation laser of 514 nm, with a spectral range between 100 cm^{-1} and 1000 cm^{-1} for the Raman spectra.
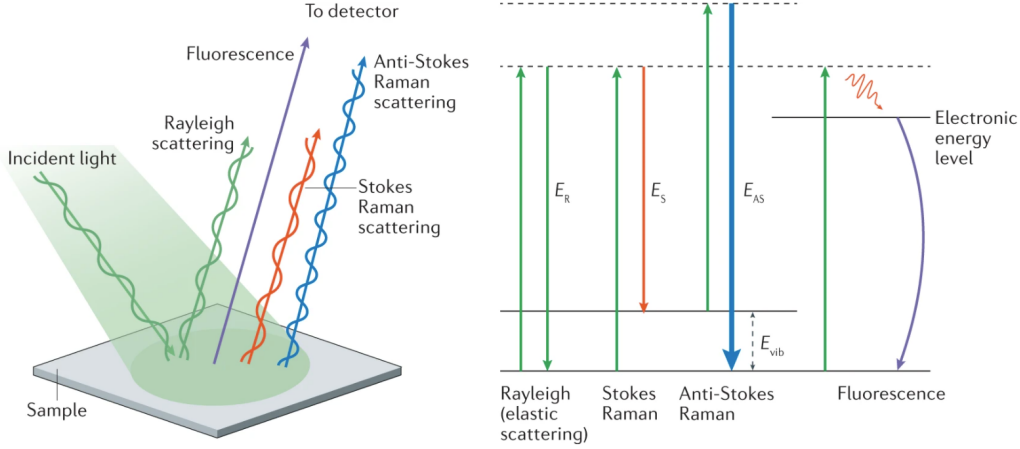
Figure 3.4: *Different scattering mechanisms that may occur upon the interaction between light and the material. The light can undergo elastic scattering (Rayleigh scattering), where the energy E_R and therefore the wavelength of the incident and scattered light remains equivalent. Inelastic scattering of the light (Raman scattering) due to vibrational oscillations results in energy transfer; the photon loses an energy E_S (Stokes shift) or obtains an energy E_{AS} (anti-Stokes shift). Adapted from[42]*

3.2.3   X-ray photoelectron spectroscopy (XPS)

X-ray photoelectron spectroscopy (XPS) is a spectroscopic technique that makes use of the photoelectric effect in order to obtain information about the composition of a thin-film sample. The irradiation of the sample by a beam of X-rays leads to the emission of photoelectrons that originate from the inner shell of the atomic orbitals. A photon from the X-ray beam with a frequency ν will transfer its energy $h\nu$ to a bound electron. If the sum of the binding energy of the electron E_B and the work function of the instrument ϕ is lower than $h\nu$, the remaining photon energy will be converted to the kinetic energy of the electron E_K. Thus, the kinetic energy of the electrons that are measured by the detector when $E_K > 0$ is given by[43]

$$E_K = h\nu - (E_B + \phi). \tag{3.5}$$

The kinetic energy of the photoelectrons provides information about the chemical composition of the surface of the material such as the chemical states, the constituent elements, and their relative abundance.[4] As the photoelectron needs to travel through the sample to reach the surface/vacuum interface, it may experience inelastic collisions, recombination, or get trapped within the material, which leads to a decrease in the intensity of the photoelectron peaks. All these mechanisms leads to an attenuation factor for the photoelectrons that are passing through the layer given by

$$I = I_0 \exp\left(-\frac{d}{\lambda \cos\theta}\right), \tag{3.6}$$

where I_0 is the signal intensity of the uncovered substrate, d is the thickness of the layer, λ is the characteristic length of the attenuation and θ is the angle of the X-ray beam with respect to the surface normal. The intensity decreases exponentially, such that the measured signal only arises from a depth of approximately 10 nm.

To determine the chemical composition of $Nb_xW_{1-x}S_2$, the experiments were performed using a Thermo Scientific^{TM} K-alpha Spectrometer that is equipped with a monochromatic Al Kα X-ray radiation source at $h\nu = 1486.6$ eV. The binding energy regions for specific elements were obtained, which are used for the quantification of the relative atomic concentrations. The XPS spectra were analyzed using the Thermo Scientific^{TM} Avantage^{TM} software. All binding energies were calibrated by taking the C_{1s} peak at 284.80 eV as the reference.

3.3   Scanning electron microscopy (SEM) and transmission electron microscopy (TEM) imaging

Electron microscopy techniques are used in order to examine the structure and morphology of the material. A beam of accelerated electrons is focused onto the sample by electromagnetic lenses and apertures. There are several types of electron microscopes, each relying on different principles. Two different electron microscopy techniques will be discussed here.

Scanning electron microscopy (SEM): Scanning electron microscopy forms an image by collecting secondary electrons, backscattered electrons, and characteristic X-rays that are emitted from the surface of the material due to interactions with the incident electron beam. The SEM images were obtained by a Zeiss Sigma microscope that operated at an acceleration voltage of 5 kV. The acquired top-view images can be investigated to obtain information about the surface morphology of the thin films.

Transmission electron microscopy (TEM): Transmission electron microscopy creates an image from the electrons that are transmitted through the film, obtaining cross-sectional top-view images of the morphology and structure of the material at atomic resolution. The cross-section TEM imaging was performed at the High Tech Campus Eindhoven on a JEOL ARM 200F Transmission Electron Microscope equipped with a 100 mm^2 Centurio SDD EDX detector that operated at 200 kV. A dual-beam focused ion beam (FIB) was used to create a thin lamella of the $Nb_xW_{1-x}S_2$ films for cross-section TEM. The films were protected during the lamella preparation by depositing a layer of SiO_2 on top using electron beam-induced deposition (EBID).

3.4 Electrical characterization techniques

3.4.1 Four-point probe (FPP)

The electrical properties of the thin-film sample can be determined by the four-point probe (FPP) method. The experiment consists of four probes with a collinear configuration, equally spaced from one another. The probes are in contact with the surface of the material, as schematically illustrated in Figure 3.5. The current is injected via the two outer probes, resulting in a voltage drop that can be measured with the two remaining probes. This way, the resistance of the sample has been determined. Then, using the dimensions of the material, the resistance can be related to the resistivity via[44]
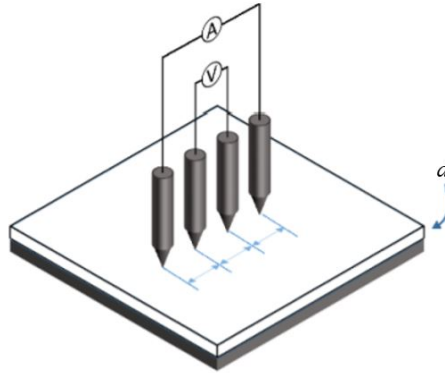
Figure 3.5: *Schematic configuration of the four-point probe (FPP) set-up. The current is injected via the outer two probes and the voltage is measured between the inner probes for a film with thickness d. Adapted from[45]*

$$\rho = \frac{RA}{L}. \tag{3.7}$$

Here, R is the bulk resistance, L is the length and A is the cross-sectional area given by the product of the width W of the sample and the thickness d. For thin-film materials, the sheet resistance R_s is used given by,

$$R_s = \frac{\rho}{d}. \tag{3.8}$$

The measurements are done on a S-301-6 Four-Point Probe station, delivered by Signatone. The set-up is connected to a Keithley 2400 sourcemeter, which has an internal resistance of 10 MΩ. This means that samples with a resistance beyond this value cannot be measured accurately.

3.4.2 Hall effect

The Hall effect is the phenomenon where a potential difference occurs across the sample upon applying a magnetic field B that is perpendicular to the surface and the direction of the current I flowing through the sample. The magnetic field exerts a Lorentz force on the charge carriers in the sample given by,

$$\vec{F} = q(\vec{E} + \vec{v} \times \vec{B}), \tag{3.9}$$

where the second term results in the charge carriers moving to the side of the material. This accumulation of charges results in a potential difference which is known as the Hall voltage V_H, which is given by

$$V_H = \frac{IB}{nqd}, \tag{3.10}$$

where n is the density of the carriers and q is the charge of the carriers. The sign of the Hall voltage V_H indicates the type of carriers that is present in the material. In case of a positive sign, the majority charge carriers in the material are holes (p-type), while for a negative sign these will be electrons (n-type). The Hall voltage can be used to determine the Hall coefficient R_H, which is an intrinsic property of the material

$$R_H = \frac{V_H d}{IB} = \frac{1}{nq}. \tag{3.11}$$

The Hall coefficient can be used to define the Hall mobility μ_H of the sample according to

$$\mu_H = \frac{|R_H|}{\rho}, \tag{3.12}$$

which in turn can be related to the drift mobility μ_d via the proportionality constant r known as the Hall factor:

$$\mu_H = r\mu_d. \tag{3.13}$$

Since the Hall factor is often unknown, it is typically taken to be unity by convention, so that the mobilities in equation 3.13 are equivalent. The experiments are conducted on a Lakeshore 8400 Series Model 8404 set-up.

An issue that occurs during the Hall measurements due to non-symmetrical positioning of the probes is the presence of a misalignment voltage V_m and a thermoelectric voltage V_{TE},

$$V = V_H + V_m + V_{TE} = \frac{IB}{nqd} + \alpha\frac{\rho}{t}I + V_{TE}, \tag{3.14}$$

where α is the misalignment factor. These error voltages can be controlled by current and field reversal. The AC mode of the Hall system is used to measure the Hall voltage. This mode generates a time-dependent magnetic field $(B(t) = B\sin(\omega t))$ such that the Hall voltage will become time-dependent as well,

$$V = \frac{\rho I}{t}(\mu B\sin(\omega t) + \alpha) + \beta\frac{dB}{dt}. \tag{3.15}$$

The use of a time-dependent magnetic field requires an additional term given by the time-derivative of the field and a constant β. Because this extra term and the misalignment voltage are independent of the magnetic field, it is possible to remove them by using a lock-in amplifier and reversing the current direction. The Hall voltage V_H and the resistivity ρ of the films are measured using a continuous magnetic field of 1.23 T and a known input current that is passing through the electrodes. The system uses the obtained parameters to determine the Hall coefficient, carrier type, carrier density, and the Hall mobility of the material.

Chapter 4

Atomic Layer Deposition of $Nb_xW_{1-x}S_2$

In this chapter, the film and growth characteristics of the ALD deposited $Nb_xW_{1-x}S_2$ alloys for different concentrations x are discussed. In Section 4.1, the results for the alloys created with the ALD supercycle process are presented. The growth, morphology and electrical properties of the films are investigated using the characterization techniques that have been described in Chapter 3. In Section 4.2, a different approach is considered for the synthesis of the alloys for very low values of x, with the aim of obtaining a better element distribution. Instead of the regular AC or BC scheme used in the ALD process for $Nb_xW_{1-x}S_2$, consisting of the precursor and co-reactant dosing steps, we now combine both schemes together to create an ABC process. Here, the ABC process is implemented in the ALD supercycle process to obtain Nb-doped WS_2 films with very low concentrations x. The films created with the ABC-supercycle (ACABC) process are compared with the standard supercycle (ACBC) process in terms of morphology and electrical properties.

4.1 Supercycle process of $Nb_xW_{1-x}S_2$

This section aims to investigate whether the film growth and composition of the $Nb_xW_{1-x}S_2$ alloys can be controlled by means of the ALD supercycle process described in Section 3.1. Experimental techniques like SE, XPS, Raman spectroscopy and SEM imaging are used to study the film characteristics and the influence of alloying on the crystallinity of the material. The electrical properties like the mobility and the resistivity of the material can be related to these changes in the composition and morphology, which are investigated by FPP and Hall measurements. Various $Nb_xW_{1-x}S_2$ compositions can be obtained upon selecting different cycle ratios [n:m]. In this case, we created a series of samples ranging from NbS_2 to WS_2: [1:0], [4:1], [1:1], [1:3], [1:9], [1:50] and [0:1]. For all the samples, a c-Si wafer that is coated with a thermally grown 450 nm SiO_2 layer is used as the substrate. Furthermore, the number of ALD cycles used per sample is varied in order to achieve a film thickness in the range between 11 to 15 nm.

4.1.1 Film growth and thickness using ALD

The apparent thickness and the growth per cycle (GPC) for the different compositions are determined by using *in-situ* SE measurements during the ALD deposition process. In Figure 4.1, the GPC of the $Nb_xW_{1-x}S_2$ films is plotted as a function of the NbS_2 cycle fraction. The growth rate for WS_2 and NbS_2 are found to be 0.78 Å and 3.1 Å per cycle, respectively, which is in agreement with values obtained from previous studies using similar processes.[19,20] For increasing NbS_2 cycle fraction, more cycles of NbS_2 are added to the supercycle ALD process and the GPC of the $Nb_xW_{1-x}S_2$ films adjust towards the GPC

of NbS_2. By fitting the rule of mixtures (Equation 3.1), it becomes apparent that the growth rate deviates from the trend for larger NbS_2 cycle fraction. In the absence of non-idealities, the film growth of the alloy should be a linear combination of the individual growth rates from the two binary materials. Since the GPC is smaller than the expected trend, this might indicate that nucleation effects occur during depositions as described in Section 3.1.1.
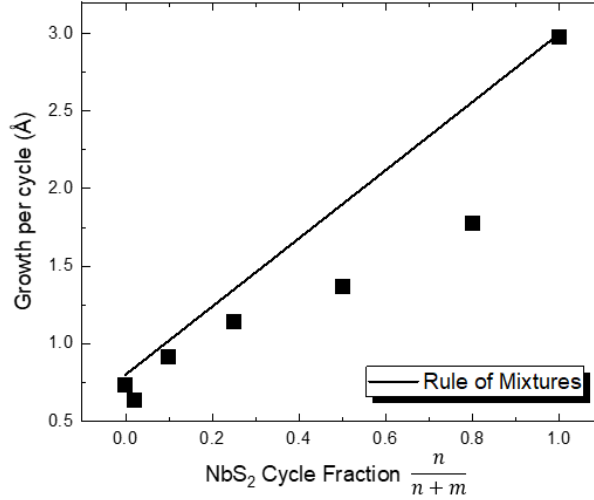

Figure 4.1: *The growth per cycle (GPC) of the different alloy compositions as a function of the NbS_2 cycle fraction.*

To further investigate this deviation, the evolution of the GPC is studied during the ALD deposition process. As the initial film growth starts with the substrate, different surface groups are present at the start of the ALD process in comparison to depositing on the material itself.[38] As a result, the first few ALD cycles will show an increase in the GPC until it reaches the maximum growth rate. For this case, the GPC is also affected by the heterogeneous deposition of the two individual materials on top of each other. Therefore, the GPC of WS_2 and NbS_2 in the ALD supercycle process of the $Nb_xW_{1-x}S_2$ films are compared with the ALD process of pure WS_2 and NbS_2 to observe any changes.

The thickness of the deposited films is plotted as a function of the number of ALD cycles, which is shown in Figure 4.2a. Here, the linear growth of the thickness for WS_2 [0:1], NbS_2 [1:0] and the cycle ratios of [1:3] and [4:1] is observed. The $Nb_xW_{1-x}S_2$ films show the alternating individual WS_2 and NbS_2 cycles during the ALD supercycle process. For the alloys, the GPC for WS_2 and NbS_2 within the supercycle process is determined by taking the slope of each individual line segment. The results are presented in Figure 4.2b. For NbS_2 and WS_2, it can be seen that the GPC reaches a value of 3.1 Å and 0.78 Å per cycle, respectively. Moreover, the growth rate of NbS_2 for the $Nb_xW_{1-x}S_2$ films has a GPC of 2.2 Å per cycle. This value is significantly lower than the GPC of 3.1 Å per cycle for the NbS_2 ALD process. The growth rate of WS_2 within the ALD supercycle process on the other hand seems to be unaffected. These results imply that NbS_2 suffers from nucleation delay when deposited on top of WS_2, causing a suppression of the growth rate. To gain

insight into changes in the film characteristics due to this deviation, the composition and morphology of the $Nb_xW_{1-x}S_2$ films are studied.
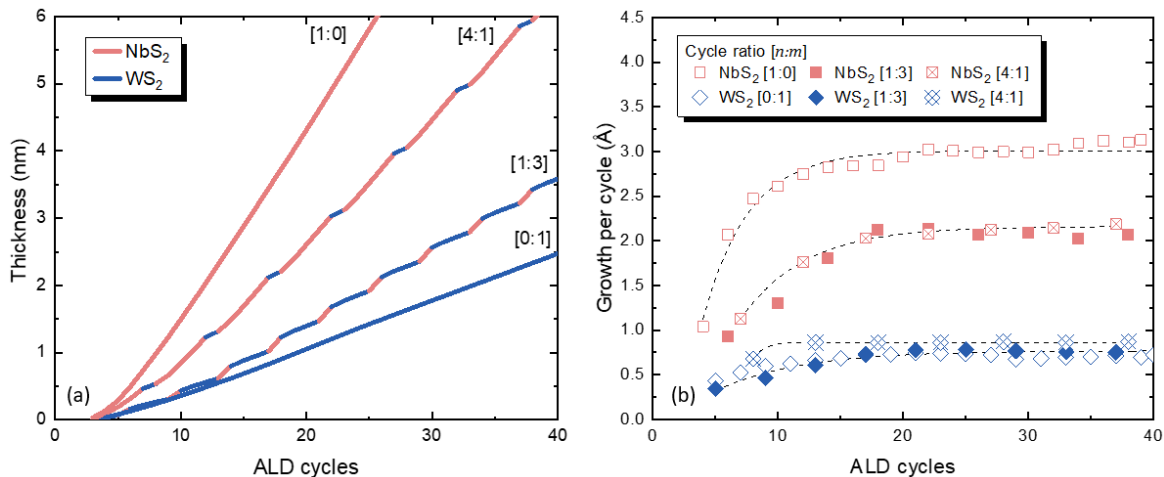

Figure 4.2: *(a) The thickness of the film as function of the number of ALD cycles for pure WS_2 [0:1] and NbS_2 [1:0] and the $Nb_xW_{1-x}S_2$ films with [4:1] and [1:3]. (b) The comparison between the GPC of pure WS_2 and NbS_2 with the $Nb_xW_{1-x}S_2$ alloys. Obtained from in-situ SE measurements.*

4.1.2   Film composition

The film composition x and the stoichiometry (sulfur-to-metal ratio) of the $Nb_xW_{1-x}S_2$ alloys are investigated by XPS analysis. The XPS spectra for the specific binding energy regions are presented in Figure 4.3. All transitions except for the 1s orbitals of an O atom exhibit a doublet peak structure. The energy shift ΔE between the peaks is due to spin-orbit coupling. The peaks can be characterized using deconvolution to find the peak position in order to find the oxidation states of the elements and the area under the peaks.

The W 4d spectrum shows the doublet peak structure consisting of the W $4d_{5/2}$ and W $4d_{3/2}$ components. The main doublet peak is located at 244.46 and 256.96 eV, indicating the presence of the W^{4+} oxidation state, which can be attributed to WS_2. The spin-orbit splitting energy ΔE between the W $4d_{5/2}$ and $4d_{3/2}$ components is found to be 12.7 $\pm$ 0.2 eV, which is in agreement with values reported in previous studies.[46] Additionally, a second doublet peak at a higher binding energy can also be observed. This second doublet peak located at 247.36 and 260.20 eV corresponds to the W^{6+} oxidation state.[47,48] The presence of these W^{6+} species indicates the formation of WO_3. As the films are exposed to ambient air, it is very likely that the surface tend to oxidize. Given that the intensity of the peaks for the W^{6+} oxidation state is much lower in comparison to the peaks of W^{4+}, this implies that only a small layer of WO_3 is formed at the surface.
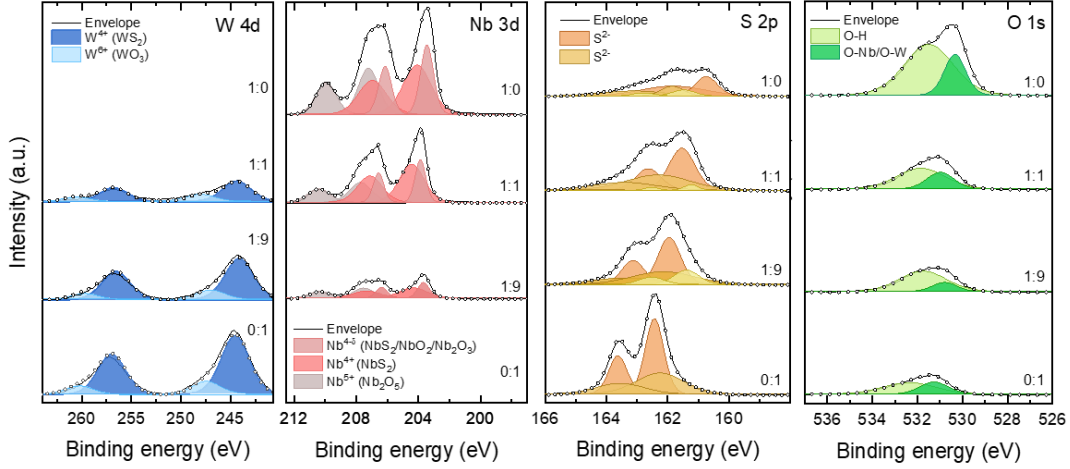
Figure 4.3: *XPS scans of the W 4d, Nb 3d, S 2p and O 1s binding energy regions for NbS$_2$ [1:0], [1:1], [1:9] and WS$_2$ [0:1]. The spectra show the intensity and the presence of different oxidation states for the given elements. The circles correspond to the raw data and the envelope indicates the fitting of the peaks.*

The Nb 3d spectrum exhibits three doublet peaks for the Nb 3d$_{5/2}$ and Nb 3d$_{3/2}$ components, corresponding to several oxidation states of Nb. The first doublet peak is located at 204.01 and 206.85 eV, which can be assigned to the presence of Nb^{4+} species that form the NbS$_2$. The splitting energy was found to be $\Delta E = 2.76 \pm 0.07$ eV, consistent with values found in literature. A second doublet peak located at 207.23 and 209.96 eV can be related to the Nb^{5+} oxidation state, which implies that Nb$_2$O$_5$ is formed at the surface.[49–52] In addition, a third doublet peak found at 203.38 and 206.08 eV corresponds to the remaining oxidation states present in the material, which are defined as Nb$^{(4-\delta)+}$ with $\delta = 1$ to 3.

Further examination is also performed on the S 2p and O 1s spectra for the different films. For the S 2p spectrum, two main doublet peaks are observed for all the different compositions given by the 2p$_{3/2}$ and 2p$_{1/2}$ orbitals. These peaks correspond to the S^{2-} species, which form the S-Nb and/or S-W bonds in the films. For the O 1s spectrum, two characteristic peaks can be seen, and these are located at 530.36 and 531.53 eV. The peak at 530.36 eV corresponds to the presence of oxygen species which form O-Nb and/or O-W bonds, so it is evident that a layer of WO$_3$ or Nb$_2$O$_5$ is formed at the surface. Furthermore, the other peak can be attributed to the presence of water adsorbed onto the surface.[20,51,53]

By inspecting all the XPS spectra, the position of the peaks tends to shift towards lower binding energies upon varying the cycle ratio from WS$_2$ [0:1] to NbS$_2$ [1:0]. This shifting indicates the downward movement of the Fermi level towards the valence band, demonstrating *p*-type doping. Previously in Section 2.1.1, it was mentioned that this effect occurs due to Nb having one electron less compared to W, which means that Nb effectively acts as a *p*-type dopant.[15,54] To obtain quantitative information from the XPS spectra, the peak areas calculated from the data are used to find the atomic fraction of the elements in the material. Prior to this calculation, the areas are normalized using a relative sensitivity factor provided by the Avantage^{TM} software. For each sample, the alloy composition x and

the sulfur stoichiometry could be determined, which is presented in Figure 4.4. Here, the composition and stoichiometry are plotted as function of the NbS_2 cycle fraction.
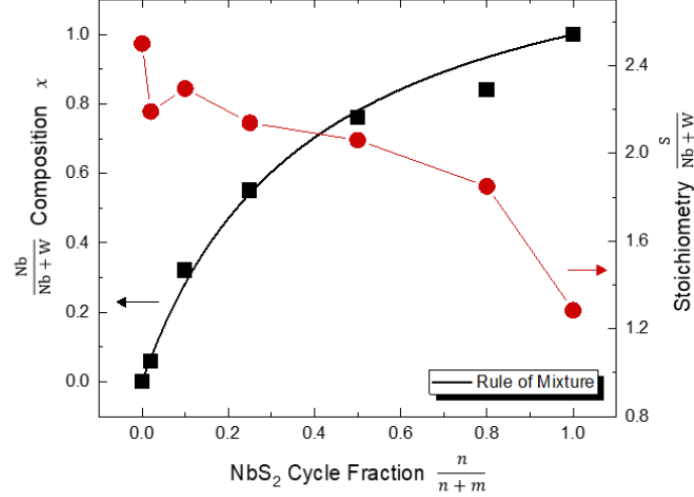

Figure 4.4: *The composition x and stoichiometry S : (Nb + W) of the different films as a function of the NbS_2 cycle fraction.*

By fitting the rule of mixtures for the alloy composition (Equation 3.2), it can be observed that the composition follows the trend for larger NbS_2 cycle fractions. It shows that the composition can be controlled upon tuning the cycle ratio for the ALD supercycle process. However, the growth rate for the $Nb_xW_{1-x}S_2$ films was not in agreement with the rule of mixtures as previously seen in Figure 4.1. This discrepancy suggests that there are changes in the morphology or the film density of the $Nb_xW_{1-x}S_2$ films in comparison to NbS_2 and WS_2. The changes in the morphology are treated in more detail in Section 4.1.3. To gain insight into the film density of the $Nb_xW_{1-x}S_2$ films, X-ray reflectivity (XRR) measurements could be performed as a follow-up research.

For the sulfur stoichiometry, increasing the concentration of Nb in the films shows a decrease in the sulfur-to-metal ratio. A value of $\sim$1.2 was found for NbS_2, which is in contrast to the values obtained by Basuvalingam.[19] In his work, a similar ALD process was used which showed a S/Nb ratio of 2.2. However, the thickness of the film that is studied in this thesis is thinner ($\sim$11 nm) in comparison to the film from literature ($\sim$30 nm). The sub-stoichiometric behavior that is observed for the NbS_2 could be due to faster surface oxidation of the films, as this became evident from the XPS spectra seen in Figure 4.3. The presence of Nb^{5+} species likely indicate Nb_2O_5 being present at the surface. The O/Nb ratio found for considering only the Nb^{5+} and O^{2-} peaks is $\sim$1.1, indicating that Nb_2O_5 is sub-stoichiometric. Since XPS is a surface sensitive technique, an overestimation in the oxygen content is possible, which could explain the low S/Nb ratio found for the NbS_2 film. Previous studies also showed that thin-film NbS_2 is prone to surface oxidization and that sample preparation is recommended in an inert environment.[55,56] The effects of the stoichiometry and composition on the film properties have been studied by examining the crystallinity and morphology of the $Nb_xW_{1-x}S_2$ films using Raman spectroscopy and SEM imaging.

4.1.3 Crystallinity and surface morphology

The initial examination on the crystallinity of the materials is done by using Raman spectroscopy. Besides finding the characteristic vibrational modes of WS_2 of NbS_2, the presence of these modes also indicate the crystallinity of the material as described in Section 3.2.2. Figure 4.5 shows the Raman spectra of the $Nb_xW_{1-x}S_2$ alloys for the different cycle ratios. All the spectra are normalized with respect to the Si peak at 520 cm^{-1}, which originates from the substrate onto which the films have been deposited. The spectrum of WS_2 [0:1] shows the characteristic peaks of the first-order Raman modes, the $E_{2g}^1(\Gamma)$ and $A_{1g}(\Gamma)$ modes, that are located at 352 cm^{-1} and 418 cm^{-1} respectively. These values are consistent with findings from literature[15,57] and indicate the growth of crystalline WS_2. Moreover, using a laser with an excitation wavelength of 514 nm also gives rise to second-order Raman peaks of WS_2. This leads to the emergence of the LA(M) mode located at 175 cm^{-1} and the 2LA(M) mode at 352 cm^{-1}. It can be seen that the 2LA(M) mode overlaps with the $E_{2g}^1(\Gamma)$ mode observed at this frequency, which causes a broadening of the peak in this region. At a cycle ratio of [1:3], the intensity of the peaks starts to decrease significantly and the $E_{2g}^1(\Gamma)$ and $A_{1g}(\Gamma)$ modes are slightly shifted towards lower wavelengths. Further increasing the concentration of Nb leads to a significant decrease in the intensity of the $E_{2g}^1(\Gamma)$ and $A_{1g}(\Gamma)$ modes of WS_2 and the emergence of small bumps located at 330 cm^{-1} and 380 cm^{-1}, which can be identified as the E_2 and A_1 modes of 3R-NbS_2. Furthermore, the presence of Nb_2O_5 could also be disclosed by identifying the characteristic modes at 228 cm^{-1} and 310 cm^{-1}. However, it is difficult to determine the presence of these peaks due to the weak signal obtained from the NbS_2 film.[58] The decrease in the intensity of the Raman peaks indicates that a transition from crystalline WS_2 to an amorphous NbS_2 film takes place, corresponding to the decrease in the sulfur stoichiometry as seen in Figure 4.4.
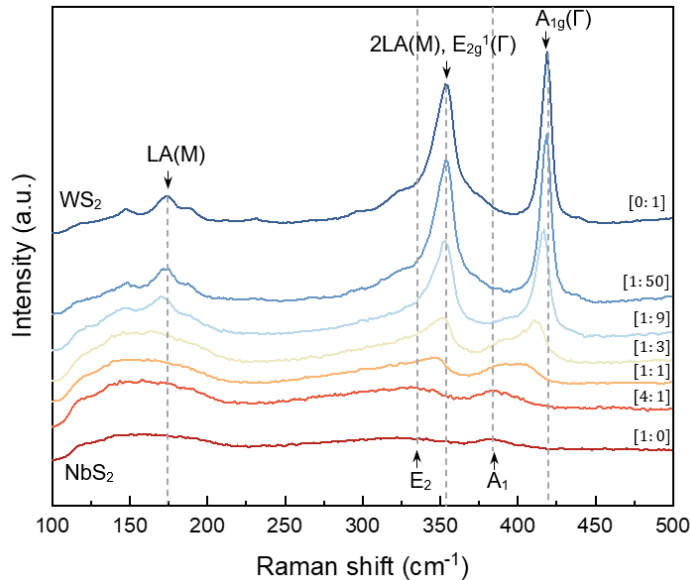

Figure 4.5: *Raman spectra of pure WS_2, NbS_2 and the $Nb_xW_{1-x}S_2$ alloys for different concentrations of x using an excitation laser with a wavelength of 514.5 nm.*

In addition to Raman spectroscopy, the surface morphology of the $Nb_xW_{1-x}S_2$ films is examined by creating top-view SEM images, which is presented in Figure 4.6. Upon initial observation, there is a clear contrast between the $Nb_xW_{1-x}S_2$ films and the WS_2 and NbS_2 films. The top-view image of NbS_2 shows a smooth surface without any rough features, which implies the growth of an amorphous film. By tuning the cycle ratio, the morphology changes and the presence of small grain-like structures with random orientations can be defined on the surface. These grains can be characterized as out-of-plane oriented (OoPO) structures, which are typically associated with crystalline growth of 2D TMDs in ALD. It shows that the crystallinity of the films improves by mixing of the two transition metal atoms. Specifically at a cycle ratio of [1:3], a high density of these OoPO structures is observed, which indicates that it exhibits a high crystallinity in comparison to the other compositions.

The deposition of a crystalline material leads to an increase in the GPC in comparison to an amorphous material, due to the presence of a crystal structure which creates spacing between the atoms. Besides, the OoPO structures also increase the surface area, which leads to more deposition of the material and an increase in the GPC as well.[20] However, the GPC seen in Figure 4.1 for the $Nb_xW_{1-x}S_2$ films does not seems to be affected by the growth of a crystalline film. In fact, a decrease in the growth rate is observed, which is a counter-intuitive result. It suggests that the nucleation delay of NbS_2 on top of WS_2 is the dominant factor that causes the decrease in the GPC. To conclude, the results of the Raman spectra and the SEM images show that the morphology of the films gradually changes from amorphous NbS_2 towards crystalline WS_2. Moreover, the growth of the crystalline films does not seem to have an influence on the GPC of the films.

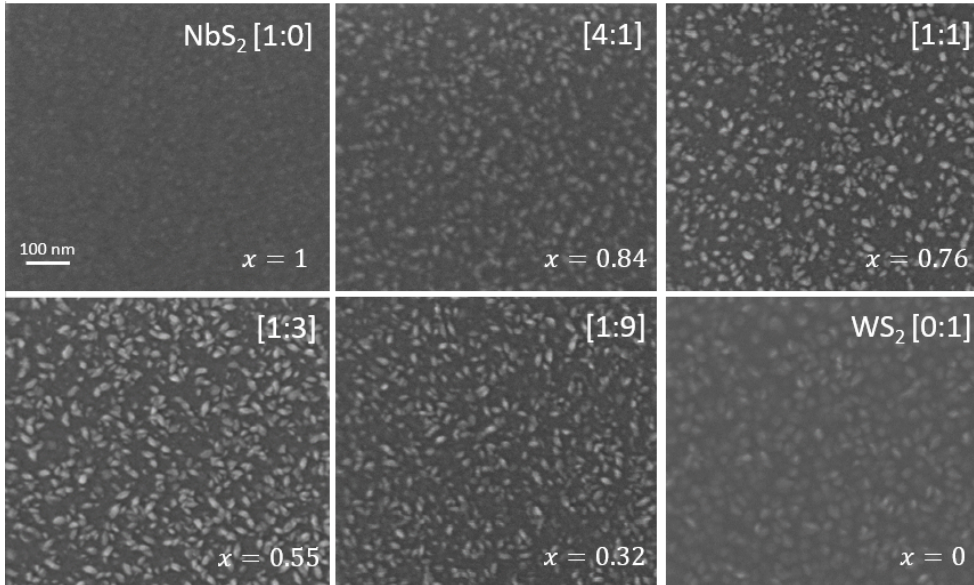**Figure 4.6:** *Top-view scanning electron microscopy (SEM) images of PE-ALD deposited $Nb_xW_{1-x}S_2$ alloys for the different cycle ratios [n:m]. Out-of-plane oriented (OoPO) structures are present at the surface for the cycle ratios of [4:1], [1:1], [1:3], [1:9], and [0:1].*

4.1.4 Electrical properties

In previous sections, the composition and morphology of the $Nb_xW_{1-x}S_2$ films was studied. The changes in the composition and morphology affect the electrical properties of the material, as will be discussed in this section. FPP and Hall measurements are performed to determine the electrical properties of the films. The resistivity of the $Nb_xW_{1-x}S_2$ films is determined by FPP measurements, which is shown in Figure 4.7. The electrical properties of WS_2 [0:1] could not be measured due to its high resistivity. Therefore, the carrier concentration and the Hall mobility could not be determined from the Hall measurements either. Starting at a cycle ratio of [1:50], the resistivity is found to be 5×10^5 µΩ cm and decreases by three orders of magnitude upon increasing the Nb concentration. The cycle ratio [4:1] shows the lowest resistivity with a value of 8.7×10^2 µΩ cm. In contrast, the resistivity is slightly larger for the NbS_2 [1:0] film. The sudden increase in the resistivity of NbS_2 can be attributed to the changes in the morphology and stoichiometry of the material. Earlier results showed that the NbS_2 film is amorphous and prone to surface oxidation, in contrast to crystalline $Nb_xW_{1-x}S_2$ films and WS_2.
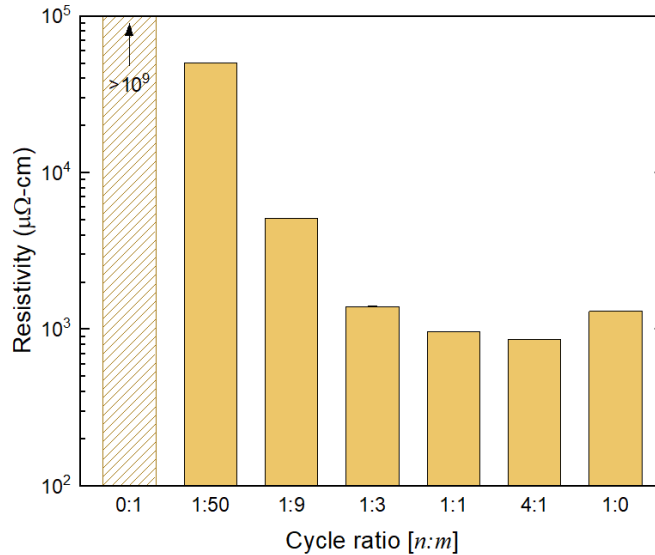
Figure 4.7: *The resistivity of the $Nb_xW_{1-x}S_2$ films plotted as function of the cycle ratio [n:m] from WS_2 [0:1] to NbS_2 [1:0].*

Hall measurements are performed to determine the carrier density n and the Hall mobility μ_H, the results of which are presented in Figure 4.8. All the samples showed p-type charge carrier characteristics upon substituting Nb on W sites. As found before in the shift of the peaks in the XPS spectra towards lower binding energies, this substitution gives rise to acceptor states in the bandgap. The electrons in the valence band will transition to these states, leaving holes behind in the valence band. This leads to free holes that become the majority charge carriers in these films. An increase in the carrier density could therefore be observed from 10^{20} to 10^{21} cm^{-3} for higher Nb concentrations. These values can be considered for degenerate semiconductors and is also close to typical values for

metals, which have a carrier density on the order of 10^{22} cm^{-3}. The carrier density for extrinsic semiconductors on the other hand is approximately 10^{17} cm^{-3}.[59] As such, the decrease in the resistivity of the films shown in Figure 4.7 can be correlated to the increase in the carrier concentration in Figure 4.8. For the Hall mobility, a value of 0.3 cm^2/Vs is found at a cycle ratio of [1:50]. For increasing Nb concentrations, the Hall mobility increases up to a maximum value of 1.7 cm^2/Vs at a cycle ratio of [1:3]. The increase in the mobility can be related to the improvement in the film crystallinity, where the film with a cycle ratio of [1:3] showed the highest density of the OoPO structures. These values are in agreement with earlier reported values in literature for the Hall mobility of NbS$_2$ in the range of 1 - 3 cm^2/Vs.[19,55] In addition, the decrease in the Hall mobility of NbS$_2$ could be due to the presence of trap states by oxygen vacancies of the sub-stoichiometric Nb$_2$O$_5$. As the pure WS$_2$ film does not seem to be affected by surface oxidation, this implies that mixing of the two transition metal atoms suppresses the formation of Nb$_2$O$_5$ and creating less of these states. It shows that surface oxidation is also a factor that influences the Hall mobility. The effect of oxidation is studied by storing three films with a cycle ratio of [1:3] each under different conditions: ambient conditions, in a glovebox and in a desiccator. After approximately two months, the Hall measurements were performed again to observe any changes in the properties. The results can be found in Appendix A.1, which show that exposure to air causes a decrease in the Hall mobility and a slight increase in the resistivity. It shows that oxidation mainly affects the mobility of these films. By performing XPS depth profiling on these samples, it can be concluded that Nb$_2$O$_5$ is indeed present at the surface of these films, which is shown in Appendix A.1.1.

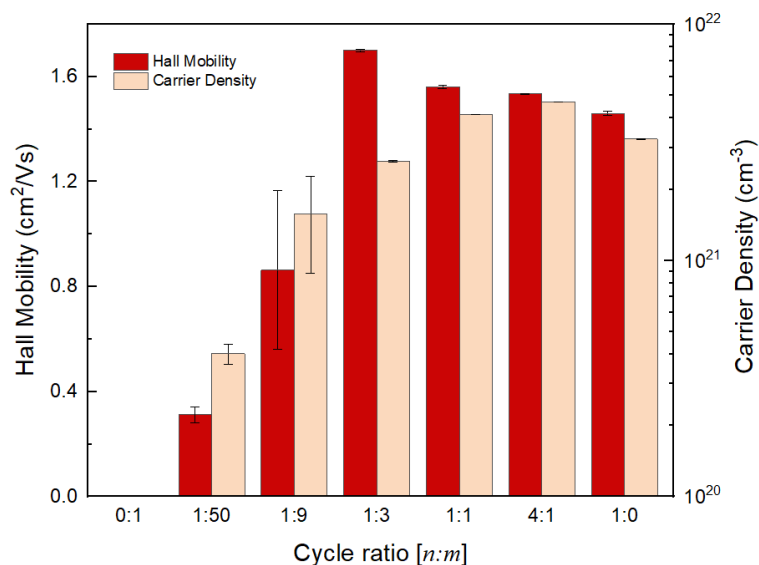**Figure 4.8:** *The Hall mobility μ_H and carrier density n of the Nb$_x$W$_{1-x}$S$_2$ alloys plotted as function of the cycle ratio [n:m] from WS$_2$ [0:1] to NbS$_2$ [1:0].*

The increase in the carrier density of the films implies that the $Nb_xW_{1-x}S_2$ films tend to exhibit metallic characteristics. To investigate the turning-point for the transition from a semiconductor to a metal, the temperature dependence of the resistivity for the films with a cycle ratio of [1:3], [1:1], [4:1] and [1:0] is measured from 120 to 300 K. The results for these measurements can be found in Appendix A.2. All the films showed a decrease in the resistivity with increasing temperature, signifying a semiconducting behavior for all the films as described in Section 2.3.2. This is in contradiction with the metallic nature of NbS_2, where an increase in the resistivity for increasing temperatures is expected.[60,61]

4.2 The ABC process of $Nb_xW_{1-x}S_2$

In general, the ALD supercycle (ACBC) process allows one to control the composition of the alloy by tuning the cycle ratio [n:m]. The GPC of the material defines the number of atoms deposited onto the surface, which makes it possible to control the composition. A large difference between the GPC of the two binary ALD processes will influence the supercycle length $n + m$. In case the growth rates of two materials are different, the number of cycles for the material with the smaller growth rate must be larger than that of the other material in order for the same number of atoms to be deposited onto the substrate. Especially in the low concentration regime for the preparation of doped thin films, the process to form these films by ALD often uses a single cycle n of the dopant atom included in m cycles for the material such that $m \gg n$. This is further enhanced by the difference in growth rates, leading to a very large supercycle length as seen in Figure 4.9.

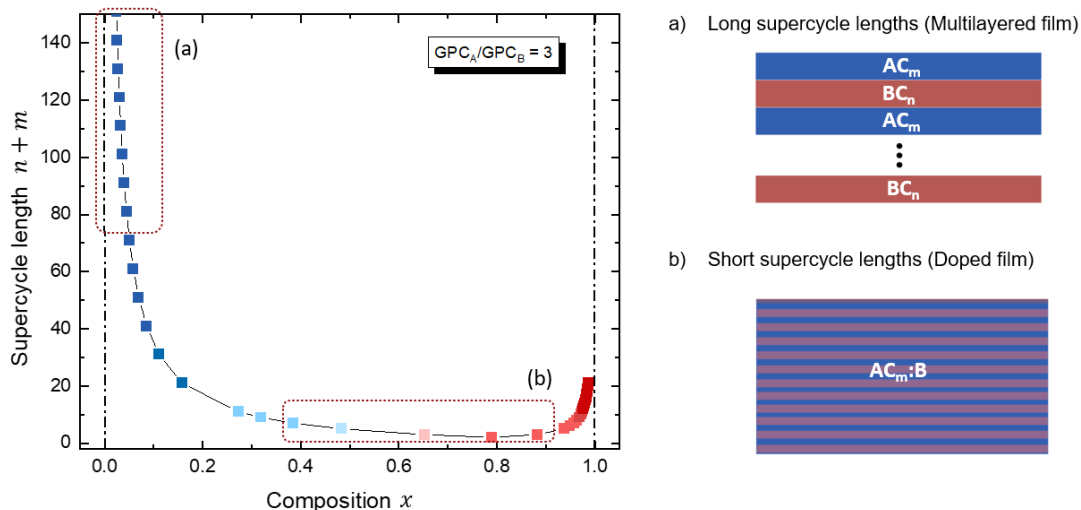**Figure 4.9:** *The supercycle length as a function of the Nb composition x, where $GPC_{NbS_2}/GPC_{WS_2} = 3$. The number of cycles needed to obtain a low-concentrated Nb film increases rapidly, leading to a multilayered film instead of a doped film. Adapted from* [38]

As stated in Section 3.1.1, large supercycle lengths result in the deposition of multilayered films, while better mixing is obtained for smaller values. Therefore, the uniformity of the dopant distribution within the film could be improved by reducing the supercycle length. To improve the dopant distribution within the material, an ABC process is developed where the precursors of the transition metal elements are dosed in sequence, followed by the co-reactant step, as shown in Figure 4.10. While the adsorption of the first precursor is the same process as for the standard ALD process, the adsorption of the second precursor onto the surface will depend on the coverage of the first precursor and the interaction between the two constituent elements.
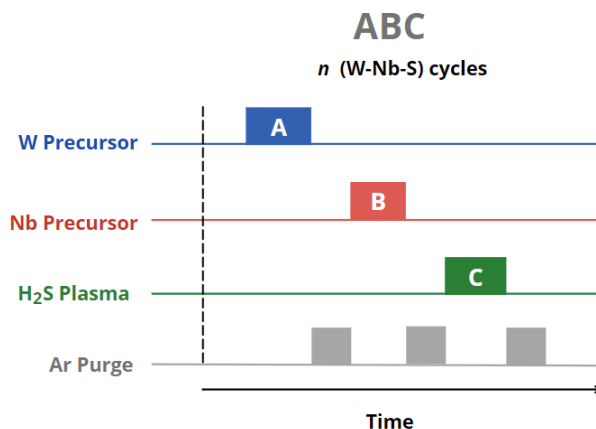
Figure 4.10: *Schematic overview of the ABC process for the PE-ALD process of* $Nb_x W_{1-x} S_2$, *where the precursors are dosed in sequence.*

The results of the composition, GPC, and the stoichiometry of the films that are created with the ABC process are presented in Table 4.1. The ABC was also changed to BAC to see whether any changes in the interactions between the two precursors can be observed, as expected. Additionally, the supercycle process (ACBC) and the ABC process are compared, from which it follows that a similar composition and stoichiometry can be obtained while using a smaller supercycle length.

Table 4.1: *The values obtained for the composition, GPC and the stoichiometry for the ABC and BAC process of* $Nb_x W_{1-x} S_2$, *compared to those of the supercycle (ACBC) process.*

Process	Length $n+m$	Composition x	GPC (Å)	Ratio S/(Nb+W)
ABC	1	0.5	1.3	2.3
ACBC	4	0.56	1.1	2.1
BAC	1	0.75	2.3	1.2
ACBC	2	0.76	1.3	2.1

A simplified illustration of the ABC process for the A and B half-cycles is shown in Figure 4.11. The surface chemistry plays a crucial role in the adsorption of the precursor. The number of active sites, the roughness of the surface, and the surface energy of the first precursor affect the saturation and thereby the growth rate of the second precursor during the ABC process. The effect on the growth rate of the second precursor was already observed in Section 4.1, where NbS_2 exhibited a lower growth rate of 2.2 Å per cycle for the supercycle process in comparison to 3.1 Å per cycle for the conventional ALD process. The results in Table 4.1 show that upon changing the sequence from ABC to BAC, the composition changes from $x = 0.5$ to 0.75 and an increase in the GPC from 1.3 to 2.3 Å per cycle is observed. To gain more insights into the surface interactions between the Nb and W precursors, follow-up research using FTIR measurements is proposed in Section 7.2.
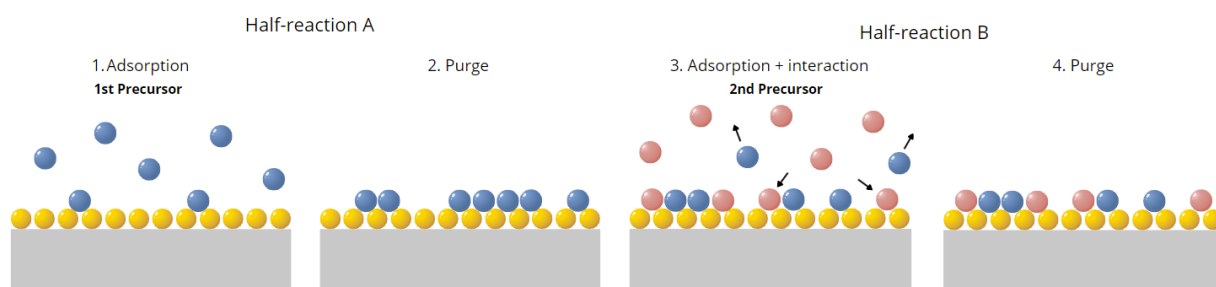
Figure 4.11: *Illustration of half-reactions A and B in the ABC process. In half-reaction A, the first precursor adsorbs onto the surface until saturation is reached. In practice, the whole surface will not be covered and there will still be some adsorption sites left. In half-reaction B, the second precursor can adsorb on the sites that are still available or displace the sites of the first precursor. The reactions are separated by a purging step.*

4.3   Supercycle process vs. ABC-supercycle process

The ABC process can be incorporated into the supercycle process, enabling short super-cycles for films with a low Nb content. The supercycle scheme for this process is shown in Figure 4.12. The effect of the supercycle length on the dopant distribution is studied for a film with $x = 0.1$. Here, the ABC-supercycle process (ACABC) is compared to the conventional supercycle process, which is seen in Table 4.2. For the conventional super-cycle (ACBC) process, a cycle ratio of [1:50] is needed, yielding a supercycle length of 51. With the ABC-supercycle process, a cycle ratio of [1 ABC : 8] is used to obtain the same composition, which means that the supercycle length is only 9. Evidently, a significantly smaller supercycle length can be used to obtain the same composition with a difference in the atomic ordering. The differences between the supercycle and ABC-supercycle process in terms of the film's morphology and electrical properties are discussed in the following sections.
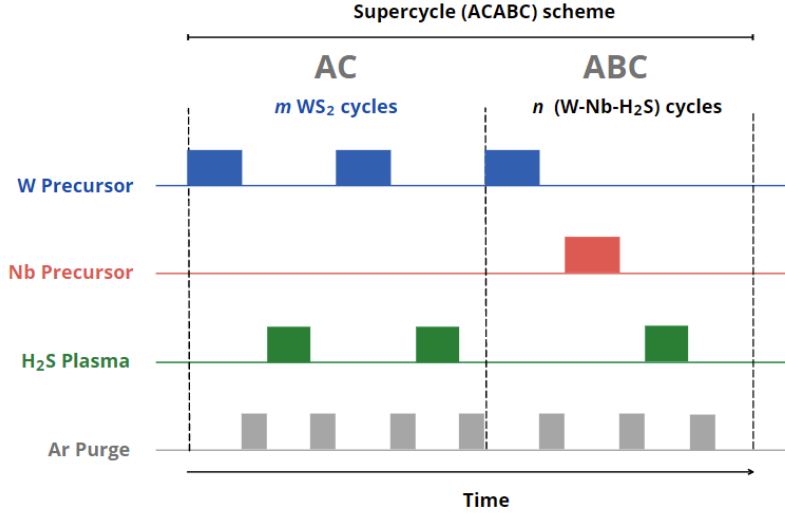
Figure 4.12: *Schematic overview of the ABC supercycle (ACABC) process for the PE-ALD process of $Nb_xW_{1-x}S_2$.*

Table 4.2: *The values obtained for the composition, GPC and stoichiometry for the $Nb_xW_{1-x}S_2$ films for the supercycle process [1:50] and the ABC-supercycle process [1 ABC : 8].*

Cycle ratio	Composition x	GPC (Å)	Stoichiometry $\frac{S}{Nb + W}$
[1:50]	0.08	0.7	2.1
[1 ABC : 8]	0.11	0.8	2.4

4.3.1 Surface morphology using TEM imaging

In order to study the morphology of the films that were formed using the two different processes, cross-sectional TEM images are taken. For the supercycle process, randomly oriented OoPO structures are present at the surface, as shown in Figure 4.13. On the other hand, less of these OoPO structures are observed for the film created with the ABC-supercycle process as seen in Figure 4.14. The GPC of WS_2 (0.71 Å per cycle) determines that 50 WS_2 cycles creates approximately five monolayers, while not even one monolayer is formed with 8 WS_2 cycles. The use of fewer WS_2 cycles might indicate that the ABC-supercycle process leads to a disruption of the WS_2 layers by earlier introducing heterogenous deposition, by depositing the Nb atoms onto the surface. This possibly leads to suppressing the formation of the OoPO structures. Furthermore, both films show distinct layers in the cross-sectional images, which indicates the deposition of a crystalline material. It shows that the ABC-supercycle process enables the growth of crystalline films with less OoPO structures.
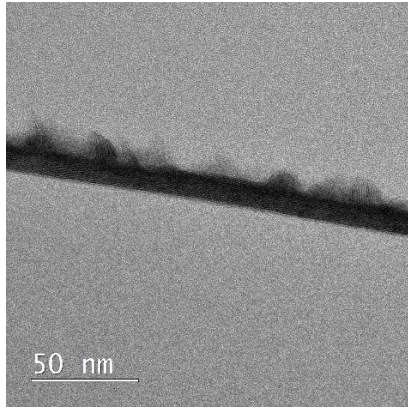
(a) *Bright-field TEM image with a scale of 50 nm.*
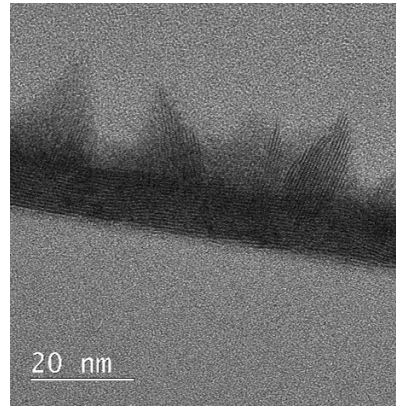
(b) *Bright-field TEM image with a scale of 20 nm.*

Figure 4.13: *Cross-sectional TEM images of the $Nb_x W_{1-x} S_2$ film [1:50] created with the supercycle process illustrating the presence of the OoPO structures at the surface and the atomic layers.*
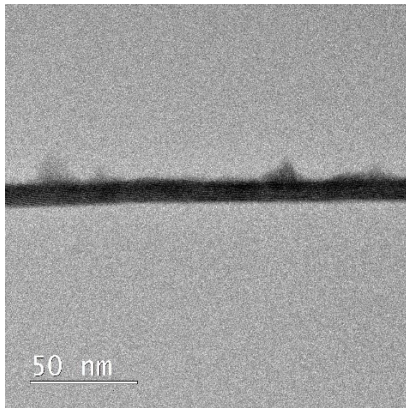
(a) *Bright-field TEM image with a scale of 50 nm.*
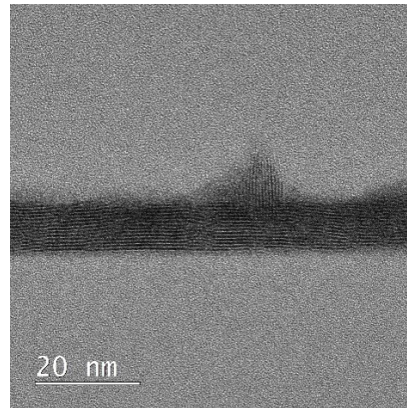
(b) *Bright-field TEM image with a scale of 20 nm.*

Figure 4.14: *Cross-sectional TEM images of the $Nb_x W_{1-x} S_2$ film [1 ABC : 8] created with the ABC-supercycle process. A lower density of OoPO structures is observed in comparison to the conventional supercycle process.*

4.3.2 Electrical properties

The electrical properties of the $Nb_x W_{1-x} S_2$ film with $x = 0.1$ are determined by using Hall measurements, the results of which are presented in Table 4.3. The film that is created using the ABC-supercycle process is found to have a resistivity that is almost two times smaller than that of the film created using the supercycle process. The Hall mobility also shows an increase by a factor of almost three. This improvement of the electrical properties of the material can be ascribed to a better distribution of the Nb dopant atoms within the film. This results in an increase in the distance between two neighboring Nb atoms such that carrier movement becomes more probable and doping becomes efficient.

Table 4.3: *The values obtained for the resistivity, Hall mobility and carrier density for the $Nb_xW_{1-x}S_2$ films for the supercycle process [1:50] and the ABC-supercycle process [1 ABC : 8].*

| Cycle ratio	ρ ($\times 10^4$ $\mu\Omega$-cm)	μ_H (cm^2/Vs)	n ($\times 10^{20}$ cm^{-3})
[1:50]	5.0	0.31 ± 0.03	4.03 ± 0.41
[1 ABC : 8]	2.6	0.77 ± 0.01	3.16 ± 0.03

4.4 Summary and discussion

The film and growth characteristics of the ALD deposited $Nb_xW_{1-x}S_2$ films have been investigated in this chapter. It shows that the GPC of the films did not follow the linear growth trend given by the rule of mixtures in Figure 4.1. The lower growth rate seems to be caused by a nucleation delay of NbS_2 on top of WS_2. This resulted that the GPC of NbS_2 in the ALD supercycle process was 2.2 Å per cycle, which is lower than 3.1 Å per cycle found for the NbS_2 ALD process. In addition, the SEM images presented in Figure 4.6 demonstrate the growth of a crystalline film for the cycle ratios of [4:1], [1:1], [1:3], [1:9] and [0:1] due to the presence of OoPO structures. The crystalline growth should lead to an increase in the growth rate for the alloys. However, this does not seem to be the case for the $Nb_xW_{1-x}S_2$ films, as the GPC values obtained are lower than expected.

On the other hand, the film composition seen in Figure 4.4 is in agreement with the rule of mixtures, indicating that the composition can be controlled by adjusting the cycle ratio. Additionally, the decrease in sulfur stoichiometry for increasing Nb concentration in the films leads to a transition from crystalline WS_2 and $Nb_xW_{1-x}S_2$ films to an amorphous NbS_2 film. The crystallinity of the films could be determined by Raman spectroscopy measurements, where the characteristic Raman modes of WS_2 could be observed but not for NbS_2. The SEM images also further supported the crystallinity of the films, where the presence of OoPO structures are visible and indicate the formation of crystalline films.

Furthermore, the electrical properties of the films are influenced by changes in the composition and morphology. The resistivity of the semiconducting WS_2 film was not measured as it was beyond the detection limit. By increasing the concentration x, a significant decrease in the resistivity by three orders of magnitude from 5×10^5 [1:50] to 8.7×10^2 $\mu\Omega$ cm [4:1] could be observed due to Nb atoms acting as a dopant and increasing the carrier density in the WS_2 film. A slight increase in the resistivity is observed for pure NbS_2, which might be affected by the presence of Nb^{5+} species that lead to the formation of sub-stoichiometric Nb_2O_5. The formation of a $Nb_xW_{1-x}S_2$ alloy seems to suppress the formation of Nb_2O_5, as WS_2 is not prone to surface oxidation. The decrease in the surface oxidation and an improvement in the crystallinity of the material implies the increase in the Hall mobility, where the largest value is observed of 1.7 cm^2/Vs for a cycle ratio of [1:3].

It was shown that in order to create a Nb-doped WS_2 film with $x = 0.1$, a cycle ratio of [1:50] was needed with the supercycle process. By using the ABC-supercycle process, a cycle ratio of [1 ABC : 8] is needed to obtain the same composition but with a smaller supercycle length. The results on the electrical properties show a decrease in the resistivity from 5.0×10^4 to 2.6×10^4 µΩ cm and an increase in the Hall mobility from 0.31 to 0.77 cm^2/Vs, which is due to the improved distribution of the Nb dopant atoms incorporated in the WS_2 film. In addition, the TEM images show that less OoPO structures are present for the cycle ratio of [1 ABC : 8]. This is likely due to less WS_2 cycles used for the ABC-supercycle process preventing the formation of multiple WS_2 monolayers stacked on top of each other.

Chapter 5

Activity of $Nb_xW_{1-x}S_2$ for the Hydrogen Evolution Reaction

The production of hydrogen gas by renewable energy sources such as wind, solar and hydropower is essential for the energy transition. Nowadays, the energy system is heavily based on fossil fuels, which have significant downsides for the climate. Several methods to obtain hydrogen have been considered, of which water electrolysis seems to be the most efficient and sustainable method.[62] This process uses electricity in order to generate oxygen and hydrogen gas from water. Additionally, electrocatalysts play a key role in the efficient energy conversion in this process. Currently, noble metals like platinum (Pt) are used as electrocatalysts for the hydrogen evolution reaction (HER) due to their high stability and their good performance, but these are not ideal in terms of cost and production.[63,64] On the other hand, 2D TMDs have shown to be promising candidates for the use as an electrocatalyst due to their large surface area, low toxicity, low costs. Moreover, the ability to modify their structural properties such as the electronic bandstructure can increase their performance for electrocatalytic activity.[65,66]

In this chapter, the electrochemical properties of the $Nb_xW_{1-x}S_2$ alloys are investigated to explore their potential as an electrocatalyst. Section 5.1 starts with the fundamental principles of the HER, describing the reactions and different reaction pathways that are taking place to form H_2 from H_2O. Additionally, several evaluation parameters such as the overpotential η and the Tafel slope are introduced, which are used to assess the HER activity of the material. In Section 5.2, a description of the experimental set-up and the measurement procedure are given. For these measurements, the $Nb_xW_{1-x}S_2$ alloys are deposited onto glassy carbon substrates by the ALD process described in Section 3.1. The results on the electrocatalytic properties are presented in Section 5.3, where a comparison is made between the alloys with different cycle ratios and literature values for WS_2 and NbS_2. Finally, the results are summarized in Section 5.4.

5.1   Theoretical background of the HER

The principle of water electrolysis is to use an electrical power source that is connected to two electrodes in order to decompose water into O_2 and H_2 gases. A schematic configuration of this set-up is shown in Figure 5.1. The electrodes are immersed in a medium consisting of water and an electrolyte (e.g. a salt, an acid, or a base). An electrolyte is needed to provide a sufficient number of ions for the reactions to take place. An electric current passes through the medium, which initiates the electrochemical reactions at these electrodes. The overall process of splitting water consists of two half-reactions: the oxygen evolution reaction (OER) at the positive electrode (anode) and the HER at the negative electrode (cathode).
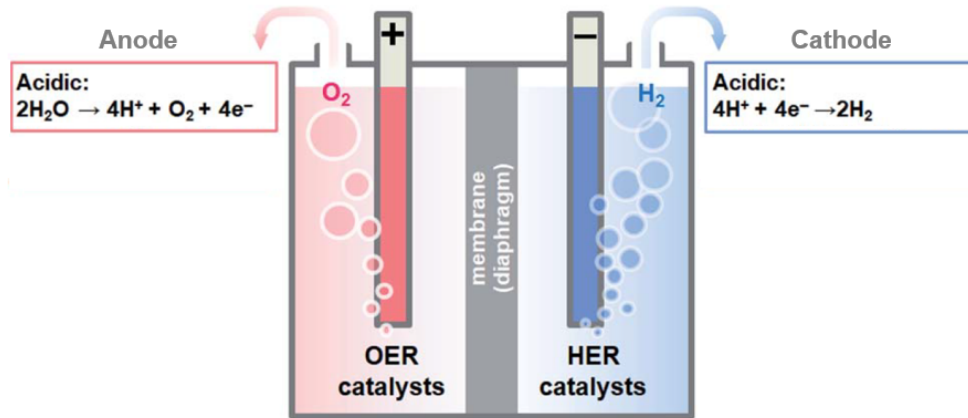
Figure 5.1: Schematic configuration of the electrolysis system consisting of the anode (red) and the cathode (blue) that are separated by a membrane in an acidic solution. The formation of O_2 happens at the anode (OER), while the formation of H_2 happens at the cathode (HER). Adapted from[64]

The general mechanism for the HER in an acidic solution consists of three reaction steps to form H_2. The first reaction is the adsorption of hydrogen ions (H^+) onto the surface sites of the catalyst. The electrons that are supplied to the catalyst will combine with the H^+ ions to form hydrogen atoms that are adsorbed onto the surface of the cathode. This reaction is known as the Volmer step, which can be written as

$$H^+ + e^- \longrightarrow H_{ads}. \tag{5.1}$$

The desorption step involves the formation of a H_2 molecule from the adsorbed hydrogen H_{ads}, which can be obtained from two reaction schemes: the Heyrovsky reaction and the Tafel reaction. The Heyrovsky reaction involves an adsorbed hydrogen atom reacting with an electron and a H^+ to form a H_2 molecule, which can be expressed as

$$H_{ads} + H^+ + e^- \longrightarrow H_2. \tag{5.2}$$

Alternatively, the Tafel reaction involves two adsorbed hydrogen atoms that will combine to form a H_2 molecule:

$$2H_{ads} \longrightarrow H_2. \tag{5.3}$$

Thus, the HER can occur via two different reaction pathways, by the Volmer-Heyrovsky (5.1-5.2) or the Volmer-Tafel (5.1-5.3) reaction. In both cases, the overall reaction scheme for the HER is given by the following reduction that takes place at the cathode

$$2\mathrm{H}^+(aq) + 2\mathrm{e}^- \longrightarrow \mathrm{H}_2\,(g). \tag{5.4}$$

Since the adsorption of hydrogen is involved in the HER, the overall reaction rate is determined by the free energy of hydrogen adsorption, ΔG_H. If the adsorption energy has a large positive value ($\Delta G_\mathrm{H} > 0$), then H^+ ions will be strongly bound to the cathode surface. As a result, it will be difficult for the Heyrosvky/Tafel reaction to take place and therefore the desorption step will limit the overall reaction rate. If the adsorption energy has a large negative value ($\Delta G_\mathrm{H} < 0$), then it is difficult for H^+ ions to be bound to the surface. This means that the adsorption step in the Volmer reaction will be the limiting factor to the reaction rate. For an ideal electrocatalyst, the value of ΔG_H should be close to thermo-neutral ($\Delta G_\mathrm{H} \approx 0$) such that H atoms neither bind too strongly nor too weakly.[20,67]

In order to assess the performance of the HER, several key parameters are considered to evaluate the efficiency of an electrocatalyst. The first important parameter is the overpotential $\eta = E - E_0$, which is the difference between the equilibrium potential E_0 and the actual potential E for a given electrochemical reaction at an electrode.[65] It is the additional voltage needed to overcome the intrinsic activation barriers that are present on the cathode and a series of resistances. In literature, the overpotential η_{10} at a current density $j = 10$ mA/cm^2 is typically used as a benchmark for the comparison of electrocatalytic materials.[62] For an electrocatalyst, the overpotential should be low in order to have a high energy efficiency. The relationship between the overpotential and the observed current density is given by the Butler-Volmer equation,[62]

$$j = j_0 \left[\exp\left(\frac{\alpha_a n F \eta}{RT} \right) - \exp\left(-\frac{\alpha_c n F \eta}{RT} \right) \right], \tag{5.5}$$

where j_0 is the exchange current density, α_a and α_c are the charge transfer coefficients of the anode and cathode respectively, n is the number of transferred electrons, F is the Faraday constant, R is the ideal gas constant and T is the temperature. As only the cathode is considered for the HER, the first term within the brackets can be neglected. With this approximation, Equation 5.5 can be rearranged to give

$$\ln j = \ln j_0 + \left(\frac{-\alpha_c n F \eta}{RT} \right). \tag{5.6}$$

By using $\ln j = 2.303 \log j$, the Tafel equation can be found. The overpotential η can be plotted as a function of the logarithm of the current density to obtain the Tafel plot, given by

$$\eta = A \cdot \log\left(\frac{j}{j_0} \right), \quad \text{where} \quad A = \frac{2.303 RT}{\alpha_c n F}. \tag{5.7}$$

The slope A in Equation 5.7, which is called the Tafel slope, is the second important parameter which determines the efficiency of the HER activity. It is inversely proportional to the charge transfer coefficient α_c, meaning that a lower Tafel slope indicates a high charge transfer across the surface of the catalyst. It therefore provides insight into the rate-determining step of the different reaction mechanisms. The theoretical slopes of the Volmer, Heyrovsky and Tafel reactions are 120, 40 and 30 mV/decade respectively.

The third parameter is the exchange current density j_0, which is the current when there is no applied potential. It defines the reduction rate of the HER at the equilibrium potential. If the exchange current density is large, then the reaction rate will be fast at the catalytic surface. The fourth parameter is the turnover frequency (TOF), which is the number of hydrogen molecules that are produced at a single active site per unit time. It is given by

$$\text{TOF} = \frac{jN_A}{n_r F N}, \tag{5.8}$$

where N_A is the Avogadro constant, n_r is the number of electrons that are consumed in the electrode reaction ($n_r = 2$ for the HER) and N is the number of active sites per unit area.[68] The last important parameter is the stability of the electrocatalyst over time, as this is essential for their long-term use in industrial applications. During this research, only the first two discussed parameters have been evaluated during this research. Several studies have already examined the electrochemical properties of WS_2 and NbS_2, presented in Table 5.1.

Table 5.1: Overview of values for the overpotential and the Tafel slope for WS_2 and NbS_2.

Material	η_{10} (mV vs. RHE)	Tafel slope (mV/decade)	Ref.
WS_2	279	81.3	[69]
WS_2	394	122	[20]
WS_2	-	164	[12]
NbS_2	530	124	[19]
NbS_2	420	-	[70]

5.2 Experimental methods

The $Nb_xW_{1-x}S_2$ films used for the electrochemical measurements were fabricated using the supercycle ALD process, which is explained in Section 3.1.1. In order to evaluate the HER performance for different alloy concentrations, pristine WS_2 and NbS_2 were used as reference samples. The films were deposited onto glassy carbon substrates with a size of 2.3×2.3 cm. These substrates are suitable for electrochemical measurements as they are highly conductive and chemically inert. Prior to the measurements, the films were stored in a glovebox with H_2O and O_2 concentrations below 0.1 ppm in order to prevent oxidation by ambient exposure. For the measurements, a three-electrode cell configuration is used instead of the two-electrode cell earlier shown in Figure 5.1. The three-electrode cell configuration makes it possible to evaluate the half-reaction of interest (HER) independently of the other half-reaction (OER). A schematic illustration of the set-up is shown in Figure 5.2, consisting of the working electrode (sample), the counter electrode and the reference electrode. A current is applied to the working and counter electrode to form the circuit. Additionally, the working electrode is typically an inert material and does not participate in the electrochemical reaction. The reference electrode has a constant potential against which the potential of the working electrode can be controlled and measured.
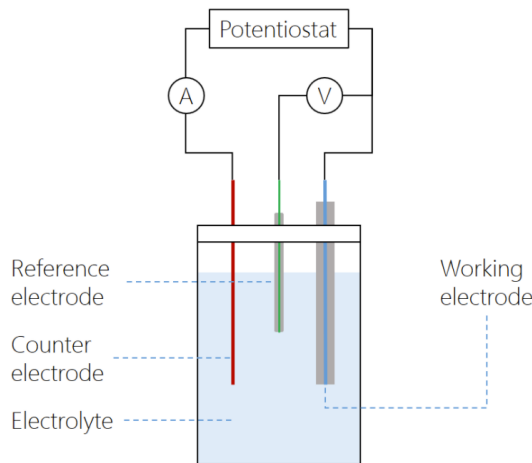

Figure 5.2: Schematic configuration of the three-electrode cell consisting of the working electrode (sample), the counter electrode and the reference electrode placed in an electrolyte. Adapted from[71]

All the measurements were performed in a three-electrode cell using a potentiostat in an acidic solution (0.5 M H_2SO_4, pH = 0.3) as the electrolyte. The samples were placed in a circular sample holder exposing an area of 3.14 cm^2, which acts as the working electrode of the system. A Ag/AgCl electrode was used as the reference electrode and a glassy carbon rod as the counter electrode. The measured potential was calibrated to a reversible hydrogen electrode (RHE) using the following equation

$$E_{\text{RHE}} = 0.228\text{V} + 0.059 \times \text{pH}. \tag{5.9}$$

Electrochemical capacitance measurements were performed by using cyclic voltammetry (CV) measurements to determine the double layer capacitance C_{dl} of the material. The double layer arises from the non-Faradaic process, where charging occurs at the interface between an electrode and the electrolyte. For the measurements, the potential of the working electrode is swept back and forth across a given potential window at a constant scan rate (mV/s) in order to locate the non-Faradaic region, where no significant changes in the current density occur as there are no charge transfer reactions taking place. The double layer capacitance C_{dl} can be related to the electrochemically active surface area (ECSA) of the films given by

$$\text{ECSA} = \frac{C_{dl}}{C_s},\qquad(5.10)$$

where C_s is the specific capacitance of the material. The ECSA represents the area of the working electrode that participates in the charge transfer of electrons and therefore in the HER.[72] Five different scan rates ranging from 50 to 250 mV/s were employed for the CV measurements and repeated two to three times for a potential range from -0.2 to 0.4 V. The scans were performed before and after the HER measurements to observe any changes in the number of active sites during the reaction. The HER performance of the films was investigated by performing five CV scans at 10 mV/s with a potential range from -0.75 to 0.2 V. To compensate for the resistance of the electrolyte, iR correction was performed. The resistance was determined from electrochemical impedance spectroscopy (EIS) measurements in the frequency range from 0.01 to 100 kHz at a open circuit potential (OCP). The overpotential η_{10} was obtained by taking the difference between the applied potential and the potential from the reference electrode (vs. RHE).

5.3   Results and discussion

Electrochemical surface area (ECSA)
The ECSA for the different alloy compositions is estimated by finding C_{dl} of the catalytic surface. The current density j is plotted as a function of the potential (V vs. RHE) from the CV scans, which is also called a polarization curve. Two examples of these curves for the alloy with a cycle ratio of [1:3] are shown in Figure 5.3a and Figure 5.4a. Similar scans have been performed for the other cycle ratios. The value for C_{dl} can be obtained by taking the non-Faradaic region of the potential for the five different scan rates. Here, the current density is taken at a potential of 0.4 V and plotted against the scan rates, shown in Figure 5.3b and 5.4b. Subsequently, a linear fit is performed to obtain the value of C_{dl}. The values of C_{dl} are obtained before and after the HER experiment for the different cycle ratios to observe whether any changes occur in the number of active sites.

A comparison between the values of C_{dl} for the $\text{Nb}_x\text{W}_{1-x}\text{S}_2$ films is shown in Figure 5.5. It must be noted that C_{dl} increases for all the different compositions, showing that the number of active sites at the surface increases by the HER. Additionally, the largest value of C_{dl} before and after the HER is found for a cycle ratio of [1:3], indicating an

increase from 0.15 to 0.2 mF/cm^2. In comparison to WS$_2$ [0:1], the value of C_{dl} for this composition is almost four times higher. The ECSA of WS$_2$ and NbS$_2$ can be evaluated using Equation 5.10. A specific capacitance of $C_s = 0.015$ mF/cm^2 for 0.5 M H$_2$SO$_2$ can be assumed to calculate the ECSA.[73] The values found for WS$_2$ and NbS$_2$ are 4 and 9.8 cm^{-2} respectively. This indicates that the number of active sites present on NbS$_2$ is two times larger than for WS$_2$. According to theoretical studies, it is expected that only the edge sites of WS$_2$ at the grain boundaries are catalytically active.[74] On the other hand, metallic TMDs like NbS$_2$ will also have catalytically active basal planes that can participate in the HER.[75] However, as C_s is merely a rough estimate, the specific capacitance for each film needs to be calculated in order to determine an accurate value for the ECSA. To obtain a better estimation for the number of active sites of the Nb$_x$W$_{1-x}$S$_2$ films, several methods are proposed which are presented in Section 7.3.
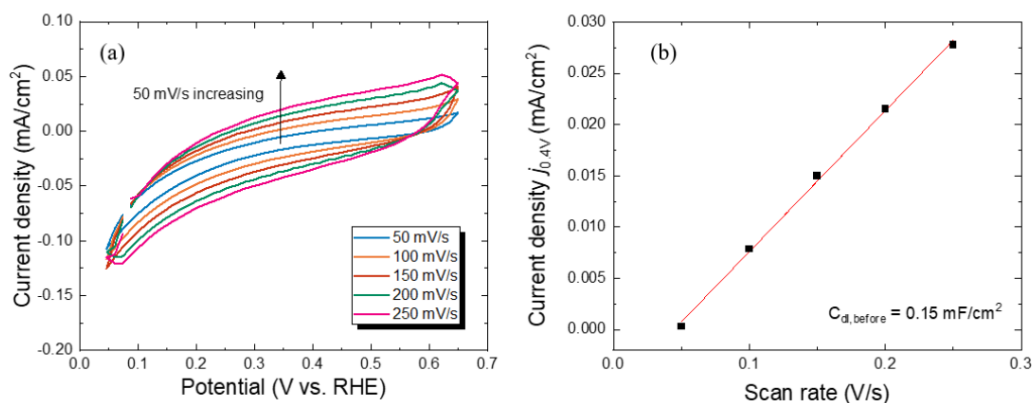

Figure 5.3: (a) CVs for five different scan rates with a cycle ratio of [1:3] and (b) the corresponding double layer capacitance C_{dl} obtained from the slope before the HER experiment.
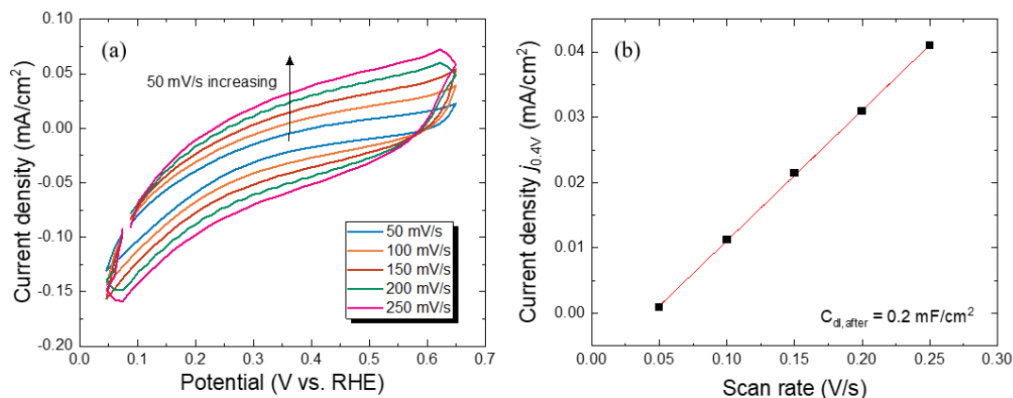

Figure 5.4: (a) CVs for five different scan rates with a cycle ratio of [1:3] and (b) the corresponding double layer capacitance C_{dl} obtained from the slope after the HER experiment.
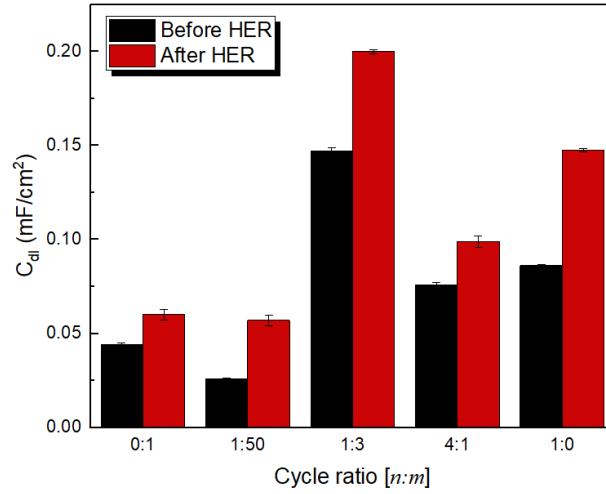
Figure 5.5: The double-layer capacitance C_{dl} before and after the HER for different compositions.

Tafel slope A and overpotential η_{10}

The HER performance of the films is investigated by performing CV scans at a scan rate of 10 mV/s. The Tafel plot and the polarization curves for the different films are presented in Figure 5.6. From the Tafel plot, the Tafel slope can be extracted by performing a linear fit around $j = 10$ mA/cm^2. According to Equation 5.7, the slope is related to the charge transfer rate of the electrons across the surface of the working electrode. A low value of the Tafel slope is desired, as this implies a high transfer coefficient α_c. Additionally, the overpotential η_{10} can be found by reading off the value of the potential at $j = 10$ mA/cm^2, which is given by the horizontal dashed line shown in Figure 5.6b. The intersection between the polarization curve and the dashed line shows that WS$_2$ and NbS$_2$ need a large potential to reach a current density of 10 mA/cm^2 in comparison to the Nb$_x$W$_{1-x}$S$_2$ films.
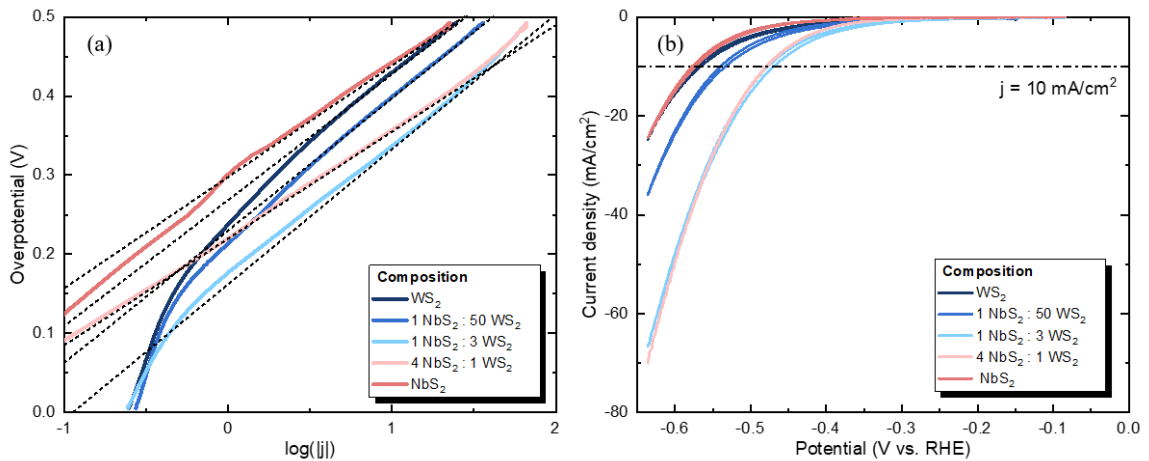

Figure 5.6: (a) The Tafel plot for the different compositions (b) CV curves for films with different compositions using a scan rate of 10 mV/s.

To provide a better overview of the results, the overpotential and Tafel slope are plotted against the composition x, which is shown in Figure 5.7. The largest value of the Tafel slope is found for WS_2, while the lowest value is found for $x = 0.84$ which corresponds to a cycle ratio of [4:1]. The values of WS_2 and NbS_2 from these composition series are found to be 161 mV/dec and 134 mV/dec respectively, which are of the same order of magnitude as the values in Table 5.1. Since the slope is inversely proportional to the charge transfer rate, this indicates that WS_2 exhibits the lowest transfer rate of electrons across the surface. Its low performance can be attributed to the very high resistivity of the film, which was observed in Section 4.1.4. Additionally, the Tafel slope shows a decrease upon increasing the concentration x. Based on these results, the decrease in the Tafel slope can be correlated to the decrease in the resistivity of the $Nb_xW_{1-x}S_2$ films as seen in Figure 4.7. The cycle ratio of [4:1] exhibits the lowest Tafel slope, which is most likely to its low resistivity. Furthermore, the lowest values for the overpotential are obtained for the $Nb_xW_{1-x}S_2$ films. Particularly, the films with a cycle ratio of [1:3] and [4:1] show a relatively small value for the overpotential of 460 and 470 mV respectively, which implies that they possess a better energy efficiency in comparison to WS_2 and NbS_2.

The electrochemical reactions can lead to changes in the composition of the $Nb_xW_{1-x}S_2$ films. To investigate these changes, XPS measurements are performed after the HER experiment, the results of which are found in Appendix B. The XPS scans show an increase in the O 1s peak, indicating that surface oxidation has taken place for all the films. For NbS_2, an increase in the intensity of the peak for the Nb^{5+} oxidation state is observed, corresponding to the possible formation of (sub)stoichiometric Nb_2O_5 at the surface. The oxidation process was mentioned in the previous chapter and was also observed in earlier studies on examining the HER performance of NbS_2.[70] However, the presence of the oxidized surface does not seem to negatively affect the electrochemical activity of NbS_2, as the number of active sites still increased after the HER measurement. Moreover, the overpotential was in a similar range as previous studies.[19,70]
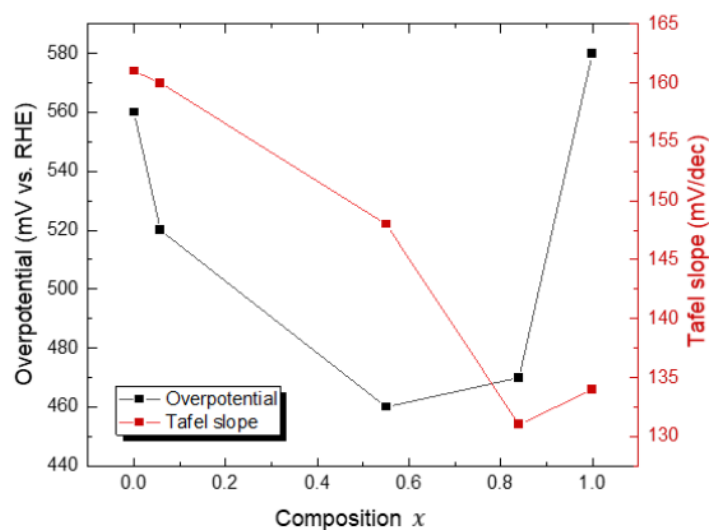

Figure 5.7: Plot of the overpotential η_{10} and the Tafel slope against the composition x.

5.3.1 Comparison of the supercycle vs. ABC-supercycle process

In Section 4.3, a comparison of the ABC-supercycle (ACABC) process and the conventional supercycle (ACBC) process was made in terms of their electrical properties. It was shown that the resistivity decreased upon employing the ABC-supercycle process and that the Hall mobility significantly improved, presumably due to an improved distribution of the Nb dopant atoms in the WS_2 film. In this section, the comparison is extended by examining the electrochemical properties of films produced by these two different processes.

The evaluation of the two processes is done by measuring the HER activity of the films deposited with cycle ratios of [1:50] and [1 ABC : 8]. The Tafel plots and the polarization curves are presented in Figure 5.8, along with the corresponding Tafel slopes and the overpotential η_{10}. The Tafel slope for the ABC-supercycle process is found to be slightly larger than the slope for the supercycle process. In the previous section, it was concluded that the decrease in the resistivity led to an improvement in the electrocatalytic properties. As the resistivity for both processes are in the same order of magnitude, this might indicate that a difference in the Tafel slope is only observed if there is a significant difference in the resistivity. Additionally, the overpotential found for both processes is almost equivalent. Based on the findings, the improved dopant distribution does not seem to significantly affect the HER performance of the material.

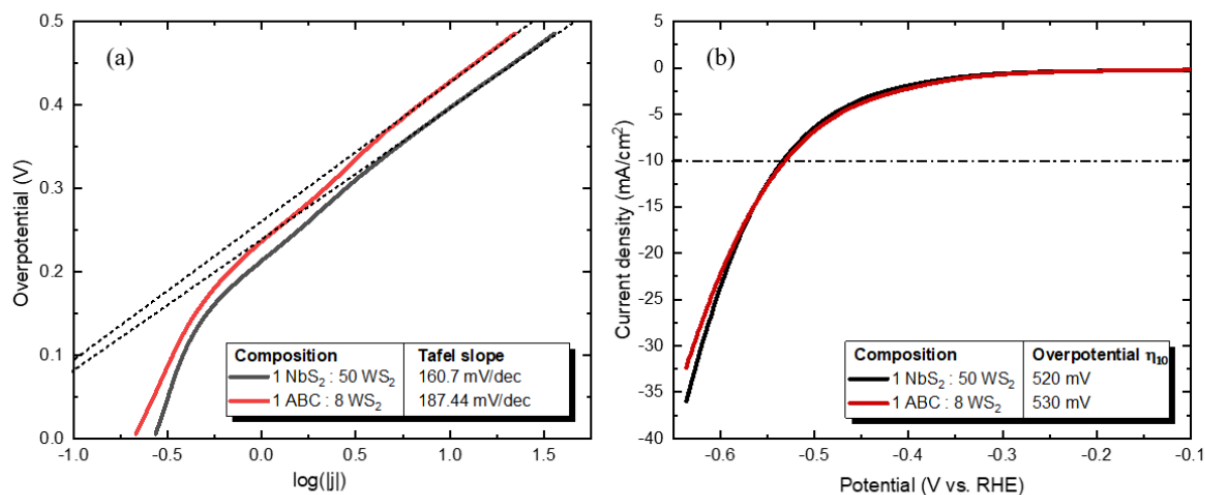**Figure 5.8:** (a) The Tafel plot for the films with a cycle ratio of [1:50] and [1 ABC : 8] with the Tafel slope found at $j = 10$ mA/cm^2 (b) CV curves for the two compositions for a scan rate of 10 mV/s and with the overpotential η_{10}.

5.4 Summary

In summary, electrochemical measurements performed on the $Nb_xW_{1-x}S_2$ alloys provide insight into their electrocatalytic properties. The overpotential η_{10} and the Tafel slope A were used as important evaluation parameters to assess the HER performance. The results of pristine WS_2 and NbS_2 have been used as a reference for comparing the alloys. The results indicate that the overpotential and the Tafel slope are smaller for the $Nb_xW_{1-x}S_2$ films with different values of x. An optimum in the HER performance was found for a cycle ratio of [4:1], corresponding to a composition of $x = 0.84$. The Tafel slope for this alloy was found to be 131 mV/dec, indicating that the rate-determining step is the Volmer reaction. Furthermore, the overpotential of this alloy was found to be 470 mV. The overall findings show that the alloys exhibit a better catalytic activity for the HER in comparison to WS_2 and NbS_2 due to improvement in the electrical properties.

Finally, the electrochemical properties of films with a composition of $x = 0.1$ that were fabricated via the supercycle process and the ABC-supercycle process are studied. In doing so, the effect of an improved doping distribution on the HER performance of the films can be determined. It was observed that the Tafel slope and overpotential were slightly larger for the films fabricated with the ABC-supercycle process, indicating that the improved dopant distribution does not affect the HER performance of the material.

Chapter 6

Conclusion

At the beginning of this thesis, several research questions were considered to achieve insight into the synthesis of $Nb_xW_{1-x}S_2$ alloys and their properties. The main focus was to investigate whether the alloy composition can be controlled with a modified ALD process. The attention was then shifted towards the electrical and electrocatalytic properties of the $Nb_xW_{1-x}S_2$ films, to observe whether an improvement in these properties could be achieved. This chapter provides answers to the first two research questions as proposed in Section 1.4.

1. Can we accurately control the alloy composition using advanced ALD deposition schemes?

To form the $Nb_xW_{1-x}S_2$ alloy, a PE-ALD supercycle process was developed that combines the individual ALD processes of WS_2 and NbS_2 from previous works. Important parameters like the cycle ratio [n:m] and the supercycle length $n + m$ were considered that define the composition and the degree of mixing of the two transition metal elements. By varying the cycle ratio, the alloy composition could be controlled and the obtained compositions are in line with the theoretically expected values from the rule of mixtures (Equation 3.2). Besides, the S/(Nb+W) ratio for the different alloy compositions show a decrease from 2.5 to 1.3 upon gradually changing from WS_2 to NbS_2. It was found that NbS_2 is prone to surface oxidation upon exposure to air. The combination of WS_2 and NbS_2 reduces the formation of an oxide layer on top of the films. In contrast with controlling the composition, the experimental GPC for the different alloy compositions exhibited a slight deviation from the predicted film growth rate (Equation 3.1). Based on the observations, it was concluded that this unexpected deviation is most likely caused by nucleation delay of NbS_2 on top of WS_2.

Insights into the crystallinity and morphology of the various alloy compositions have been obtained by Raman spectroscopy and by taking SEM images. The Raman spectrum of pure WS_2 shows the characteristic Raman modes E_{2g}^1 and A_{1g}, which indicates that crystalline WS_2 is formed. Upon gradually changing the composition x to higher Nb concentrations, the intensity of the peaks decreases and a shift towards lower wavenumbers is observed. The decrease in the intensity indicates the reduction in the crystallinity of the films. This conclusion is further supported by top-view SEM images that show the presence of OoPO structures, which are a measure of the crystallinity of a material.

The large difference in the GPC of WS_2 and NbS_2 ($GPC_{NbS_2}/GPC_{WS_2} \approx 3$) means that a large supercycle length is required for small values of x. As a result, the degree of mixing of the two transition metal atoms is negatively affected. To improve the distribution of the elements within the film, an ABC process was developed in which the precursors of W and

Nb are subsequently dosed, followed by a H_2S co-reactant step. The results for $x = 0.1$ show an improvement in the electrical properties upon including the ABC process into the supercycle process: a decrease in the resistivity from 5×10^4 to 2.6×10^4 $\mu\Omega$ cm and an increase in the Hall mobility from 0.31 to 0.77 cm^2/Vs. To conclude, the ABC process is a promising way to improve the distribution of the elements for low x regimes when there is a large difference in the GPC.

2. Can we improve the catalytic activity of WS$_2$ and NbS$_2$ by synthesizing a Nb$_x$W$_{1-x}$S$_2$ alloy?

The electrochemical properties of the Nb$_x$W$_{1-x}$S$_2$ alloys have been investigated by performing HER measurements. Several parameters like the Tafel slope and the overpotential were determined to evaluate their catalytic properties. The Tafel slope indicates the charge transfer kinetics for the HER reaction, while the overpotential is used to assess the efficiency of the electrocatalyst. For an ideal catalyst, a low Tafel slope and overpotential are desired. The Nb$_x$W$_{1-x}$S$_2$ film with a cycle ratio of [4:1] showed the lowest Tafel slope of 148 mV/dec. In addition, the overpotential η_{10} was found to be 470 mV, which outperforms the catalytic properties of WS$_2$ and NbS$_2$ within this composition series. The improvement of the catalytic properties can be attributed to a reduction in the charge transfer resistance, which the electrons will experience when traveling across the surface.

3. Can we achieve a 2D TMD alloy with electrical properties suitable for the implementation in field-effect transistors (FETs)?

The results on the electrical properties of the Nb$_x$W$_{1-x}$S$_2$ alloys have obtained from FPP and Hall measurements. The resistivity, carrier density, and Hall mobility changed with the composition x. As such, these properties can be optimized by tuning the cycle ratio. The smallest value of the resistivity was found to be 8.7×10^2 $\mu\Omega$ cm at a cycle ratio of [4:1], which is attributed to an increase in the carrier concentration. Furthermore, the largest measured value of the Hall mobility was 1.7 cm^2/Vs at a cycle ratio of [1:3], which can be correlated to an improvement in the crystallinity and reduced surface oxidation of the film. These results show that Nb$_x$W$_{1-x}$S$_2$ alloy could be a promising candidate to be used as a channel region in FETs. The manufacturing and characterization of FET devices based on the Nb$_x$W$_{1-x}$S$_2$ films are currently in progress and a motivation to fabricate these devices is elaborated in Section 7.1 in the outlook.

Chapter 7

Outlook

While the formation of the $Nb_xW_{1-x}S_2$ alloy has been realized in this thesis, follow-up research would be recommended to investigate the synthesis of this material, as well as its properties, in further detail. In the following sections, some follow-up experiments are proposed which will be able to complement the results from this thesis.

7.1 Device fabrication of $Nb_xW_{1-x}S_2$ FETs

Among the various semiconducting TMDs, WS_2 is a promising candidate as a channel material for FETs. Theoretical calculations show that the carrier mobility is over 1000 cm^2/Vs due to its low effective mass.[76,77] However, reported studies have shown that the mobility is limited by Coulomb impurities, charge traps, surface defects, and roughness. Due to these effects, the mobility is lower as it is stated in theory. The metallic nature of NbS_2 leads to an improvement in the electrical transport properties of WS_2 and can be considered as a method to realize its practical application for FETs. In addition, the charge carriers injected through the source electrode will come across the metal-semiconductor interface to reach the channel to move towards the drain electrode. The contact resistance R_c that the carriers will experience between the electrode and the channel is due to the formation of a Schottky barrier; a potential barrier that limits the movement of the carriers. Earlier reported studies show that the incorporation of Nb atoms in the WS_2 layer can lead to the reduction in the Schottky barrier due to an increase in the hole concentration and improvements at the metal-semiconductor interface due to the metallic characteristics of Nb that are incorporated in the channel material.[14,15,78] This is another reason to further study $Nb_xW_{1-x}S_2$ devices, in particular the contact resistance.

7.2 Research on the surface interactions

The ABC-supercycle process where two metal-organic precursors are dosed in sequence has led to some intriguing results upon inverting the order of steps, from ABC to BAC. Analyzing transmission Fourier-transform infrared (FTIR) spectra could make it possible to understand the surface chemistry that takes place at the interface. The results can give insights into the interactions between the precursors and also at the surface of the substrate. The principle of FTIR spectroscopy relies on the absorption and transmission of infrared light upon passing through the sample. Every bond or ligand of the molecule will absorb the infrared light at a specific frequency. By measuring these frequencies, an absorbance spectrum can be obtained with characteristic peaks that lead to the qualitative analysis of the ligands which remain at the substrate surface and which that have been removed. By analyzing this spectrum, it is possible to determine which ligands are present

on the substrate surface, and which have been removed. Upon adsorption of the ligands at the substrate surface, a positive peak will be observed, whereas the removal of chemical species leads to negative peaks in the spectrum.

However, before it is possible to analyze the films using FTIR spectroscopy, the infrared spectrum of the individual precursor molecules of Nb and W needs to be determined. Since both precursors contain the tert-butylimido (N-C_4H_9) type ligands, it would be difficult to distinguish their spectra if they remain on the surface after deposition. The difference between the BTBMW and TBTDEN precursors is that the former contains the dimethylamido (N-$(CH_3)_2$) ligands and the latter the diethylamido (N-$(C_2H_5)_2$) ligands.

7.3 Research on the HER performance

Results of the electrochemical measurements show an improvement of the catalytic properties of the $Nb_xW_{1-x}S_2$ alloys compared to WS_2 and NbS_2. In order to get a more complete understanding about the catalytic properties of $Nb_xW_{1-x}S_2$, it is crucial to assess the evaluation parameters that have not been considered in this thesis. One of these evaluation parameters is the long-term stability of the alloys, which is used to observe if their electrocatalytic performance degrade over time. The long-term stability can be assessed by conducting a larger number of cyclic voltammetry cycles, e.g. 1000, and subsequently measuring the new polarization curves.

The turnover frequency (TOF), which is the number of hydrogen molecules produced per active site per unit time, could also be determined. To this end, the total number of active sites N that are present at the surface of the catalyst is required. Shin et $al.$[68] determined the active sites N using the following equation,

$$N = R_f \left(\frac{N_A d}{M} \right)^{2/3},$$ (7.1)

where it is assumed that the film structure and the film properties are isotropic. In this equation, R_f is the surface roughness factor which is defined as the ratio between the real surface area and the geometric area, N_A is Avogadro's constant, d is the film density and M is the formula weight of the molecule. The value for the film density d can be obtained using various techniques, like grazing incidence X-ray reflectivity (XRR). The roughness factor R_f depends on the surface topography of the material, which can be quantitatively studied using atomic force microscopy (AFM).

A commonly used method to measure and analyze the specific surface area of a material is by the Brunauer-Emmett-Teller (BET) method. The principle is based on the adsorption of unreactive gas species onto the surface for the quantification of the specific surface area. Typically, the BET method is conducted by using N_2 gas.[79] The BET equation is given by

$$\frac{1}{v[(p_0/p) - 1]} = \frac{c-1}{v_m c} \left(\frac{p}{p_0} \right) + \frac{1}{v_m c},$$ (7.2)

where v is the adsorbed gas quantity, p_0 and p are the saturation and equilibrium pressure of the gas, respectively, c is the BET constant and v_m is the volume of the amount of required to form a monolayer. By measuring the amount of the adsorbed gas onto the surface as a function of its pressure at a constant temperature, a straight line can be observed. The slope in this linear region gives the quantities of v_m and c. The value of v_m can be used to calculate the total surface area, which is given by the following equation

$$S_{tot} = \frac{v_m N_A s}{V},\tag{7.3}$$

with s the adsorption cross section and V is the molar volume of the adsorbate gas. The specific surface area S_{BET} can be determined from the total surface area divided by the mass of the sample a,

$$S_{BET} = \frac{S_{tot}}{a}.\tag{7.4}$$

Anantharaj et al.[80] proposed several other methods for calculating the exact number of active sites and to study in-situ structural changes at the catalytic surface. The first technique introduces UV/Vis/Raman/IR-active probe molecules in the electrolyte that have the capability to adsorb onto the catalyst surface. The absorption/reflection/transmittance values of the free probe molecules in the electrolyte at open-circuit voltage (OCV) provide an indication of the concentration of probe molecules adsorbed onto the surface. A second technique to study the surface topography of the catalyst is by microscopy techniques such as AFM or scanning tunneling microscopy (STM). Electrochemical AFM (EC-AFM) performs in-situ AFM measurements during the electrochemical reaction, allowing to study structural changes that occur at the surface. In EC-AFM, a standard AFM set-up is equipped with a three-electrode electrochemical cell. The AFM tip is placed on top of the surface of the working electrode that is immersed in an electrolyte solution.[81] A similar set-up is required for electrochemical STM (EC-STM), except an additional requirement is that a bipotentiostat is needed to independently control the potential at the tip and at the working electrode.[82]

Bibliography

[1] Kolobov, A.V. and Tominaga, J. *Two-Dimensional Transition-Metal Dichalcogenides*, volume 239. Springer, 2016.

[2] Peng, B., Zheng, W., Qin, J.T., and Zhang, W.L. Two-Dimensional MX_2 Semiconductors for Sub-5 nm Junctionless Field Effect Transistors. *Materials*, 11:430, 2018.

[3] Li, M.Y., Su, S.K., Wong, H.S.P., and Li, L.J. How 2D semiconductors could extend Moore's law. *Nature*, 2019.

[4] Samadi, M., Sarikhani, N., Zirak, M., Zhang, H., Zhang, H.L., and Moshfegh, A.Z. Group 6 Transition Metal Dichalcogenide. *Nanoscale Horizon*, 3:90, 2018.

[5] Wolf, E.L. *Applications of Graphene: An Overview*. Springer, 2014.

[6] Choi, W.B., Choudhary, N., Han, G.H., Park, J.H., Akinwande, D., and Lee, Y.H. Recent development of two-dimensional transition metal dichalcogenides and their applications. *Materials Today*, 20(3):653–671, 2017.

[7] Duan, X.D., Wang, C., Pan, A.L., Yu, R.Q., and Duan, X.F. Two-dimensional transition metal dichalcogenides as atomically thin semiconductors: opportunities and challenges. *Chem. Soc. Rev.*, 44:8859–8876, 2015.

[8] Arul, N.S. and Nithya, V.D. *Two Dimensional Transition Metal Dichalcogenides: Synthesis, Properties, and Applications*. Springer, 2019.

[9] Barua, S., Dutta, H.S., Gogoi, S., Devi, R., and Khan, R. Nanostructured MoS2-Based Advanced Biosensors: A Review. *ACS Appl. Nano. Mater.*, 1:2–25, 2018.

[10] Zhang, Y., Tin, L., Chu, J.W., Shifa, T.A., Xia, J., Wang, F., Wen, Y., Zhan, X.Y., Wang, Z.X., and He, J. Edge-Epitaxial Growth of 2D NbS_2-WS_2 Lateral Metal-Semiconductor Heterostructures. *Adv. Mater.*, 30, 2018.

[11] Voiry, D., Yang, J.E., and Chhowalla, M. Recent Strategies for Improving the Catalytic Activity of 2D TMD Nanosheets Toward the Hydrogen Evolution Reaction. *Materials*, 28, 2016.

[12] Pam, E.R., Hu, J.P., Ang, Y.S., Huang, S.Z., Kong, D.Z., Shi, Y.M., Zhao, X.X., Geng, D.C., Pennycook, S.J., Ang, L.K., and Yang, H.Y. High-Concentration Niobium-Substituted WS_2 Basal Domains with Reconfigured Electronic Band Structure for Hydrogen Evolution Reaction. *ACS Appl. Mater. Interfaces*, 11:34862–34868, 2019.

[13] Wang, L., Hu, P., Long, Y., Liu, Z., and He, X.X. Recent advances in ternary two-dimensional materials: synthesis, properties and applications. *J. Mater. Chem. A*, 5:22855–22876, 2017.

[14] Jin, Y.Y., Zeng, Z.Y., Xu, Z.W., Lin, Y.C., Bi, K.X., Shao, G.L., Hu, T.S., Wang S.S., Li, S.S., Suenaga, K., Duan, H.G., Feng, Y.X., and Liu, S. Synthesis and Transport Properties of Degenerate P-Type Nb-Doped WS_2 Monolayers. *Chem. Mater.*, 31:3534–3541, 2019.

[15] Feng, P.L., Jiang, W.Z., Su, J., Zhou, L.Q., and Liu, Z.T. Performance of field-effect transistors based on $Nb_xW_{1x}S_2$ monolayers. *Nanoscale*, 8:6507, 2016.

[16] Mackus, A.J.M., Kessels, W.M.M., and Vos, M.F.J. Atomic Layer Deposition Process Development – 10 steps to successfully develop, optimize and characterize ALD recipes. *AtomicLimits*, 3, 2019.

[17] Knoops, H.C.M., Potts, S.E., Bol. A.A., and Kessels, W.M.M. *Atomic Layer Deposition*. Handbook of Crystal Growth, 2015. Chapter 27.

[18] Sasaki, S., Kobayashi, Y., Liu, Z., Suenaga, K., Maniwa, Y., Miyauchi, Y., and Miyata, Y. Growth and optical properties of Nb-doped WS_2 monolayers. *Appl. Phys. Express*, 9:071201, 2016.

[19] Basuvalingam, S.B. *Atomic Layer Deposition of Low-Dimensional Transition Metal Di- and Tri- Chalcogenides and their Heterostructures*. PhD thesis, Eindhoven University of Technology, 2020.

[20] Balasubramanyam, S. *Nanoengineering of two-dimensional WS_2 by Atomic Layer Deposition*. PhD thesis, Eindhoven University of Technology, 2020.

[21] Zhang, X., Qiao, X.F., Shi, W., Wu, J.B., Jiang, D.S., and Tan, P.H. Phonon and Raman scattering of two-dimensional transition metal dichalcogenides from monolayer, multilayer to bulk material. *Chem. Soc. Rev.*, 44:2757–2785, 2014.

[22] Sun, Y., Wang, D., and Shuai, Z. Indirect-to-Direct Band Gap Crossover in Few-Layer Transition Metal Dichalcogenides: A Theoretical Prediction. *J. Phys. Chem. C*, 120:21866–21870, 2016.

[23] Kuc, A., Zibouche, N., and Heine, T. Influence of quantum confinement on the electronic structure of the transition metal sulfide TS_2. *physical Review B.*, 83, 2011.

[24] Kutana, A., Penev, E.S., and Yakobson, B.I. Engineering electronic properties of layered transition-metal dichalcogenide compounds through alloying. *Nanoscale*, 6:5820, 2014.

[25] Xie, L.M. Two-dimensional transition metal dichalcogenide alloys: preparation, characterization and applications. *Nanoscale*, 7:18392–18401, 2015.

[26] Li, N., Liu, Z.T., Hu, S.L., and Wang, H.Q. Structural and electronic properties of effective p-type doping WS2 monolayers: A computational study. *Solid State Communications*, 269:58–63, 2018.

[27] Gao, J., Kim, Y.D., Liang, L., Idrobo, J.C., Chow, P., Tan, J., Li, B., Li, L., Sumpter, B.G., Lu, T.M., Meunier, V., Hone, J., and Koratkar, N. Substitutional doping in 2D transition metal dichalcogenides. *Adv. Mater.*, 28:9735–9743, 2016.

[28] Tan, P.H. *Raman Spectroscopy of Two-Dimensional Materials*. Springer, 2019.

[29] Zhang, X., Tan, Q.H., Wu, J.B., Shi, W., and Tan, P.H. Review on the Raman spectroscopy of different types of layered materials. *Nanoscale*, 8:6435, 2016.

[30] McMullan, W.G. and Irwin, J.C. Raman Scattering from 2H and 3R-NbS$_2$. *Solid State Communications*, 45:557–560, 1983.

[31] Berkdemir, A., Gutiérrez, H.R., Botello-Méndez, A.R., Perea-López, N., Elías, A.L., Chia, C.I., Wang, B., Crespi, V.H., López-Urías, F, Charlier, J.C., Terrones, H., and Terrones, M. Identification of individual and few layers of WS$_2$ using Raman Spectroscopy. *Sci. Rep*, 3:1755, 2013.

[32] Liang, F., Xu, H., Wu, X., Wang, C., Luo, C., and Zhang, J. Raman spectroscopy characterization of two-dimensional materials. *Chin. Phys. B.*, 27, 2018.

[33] Yu, P. and Cardona, M. *Fundamentals of Semiconductors*. Springer, 2010. Fourth Edition.

[34] Khan, K., Tareen, A.K., Aslam, M., Wang, R., Zhang, Y., Mahmood, A., Ouyang, Z., Zhang, H., and Guo, Z. Recent developments in emerging twodimensional materials and their applications. *J. Mater. Chem. C.*, 8:387, 2020.

[35] Askeland, D.R., Fulay, P.P., and Wright, W.J. *The Science and Engineering of Materials*. Global Engineering, 2010.

[36] Kasap, S. and Capper, P. *Handbook of Electronic and Photonic Materials*. Springer, 2007.

[37] Knoops, H.C.M., Baggetto, L., Langereis, E., Sanden, van de, M.C.M., Klootwijk, J.H., Roozeboom, F., Niessen, R.A.H., Notten, P.H.L., and Kessels, W.M.M. Deposition of TiN and TaN by Remote Plasma ALD for Cu and Li Diffusion Barrier Applications. *Journal of the Electrochemical Society*, 155(12):287–294, 2008.

[38] Mackus, A.J.M., Schneider, J.R., MacIsaac, C., Baker, J.G., and Bent, S.F. Synthesis of Doped, Ternary, and Quaternary Materials by Atomic Layer Deposition: A Review. *Chem. Mater.*, 31:1142–1183, 2019.

[39] Dorywalski, K., Maciejewski, I., and Krzyzynski, T. Spectroscopic ellipsometry technique as a materials characterization tool for mechatronic systems — The case of composition and doping concentration monitoring in SBN crystals. *Mechatronics*, 37:33–41, 2016.

[40] Tompkins, H.G. and Hilfiker, J.N. *Spectroscopic Ellipsometry: Practical Application to Thin Film Characterization.* Momentum Press, 2016.

[41] Das, S. and Agraal,Y.K. Raman spectroscopy: Recent advancements, techniques and applications. *Vibrational Spectroscopy*, 57:163–176, 2011.

[42] Mosca, S., Conti, C., Stone, N., and Matousek, P. Spatially offset Raman spectroscopy. *Nat Rev Methods Primers*, 1:21, 2021.

[43] Watts, J.F. X-ray photoelectron spectroscopy. *Materials Science and Engineering*, pages 653–671, 1994.

[44] McGuire, G.E. and Strausser, Y. *Characterization in Compound Semiconductor Processing.* Momentum Press, 1995.

[45] Balestrieri, B. Transparent conductive oxides with photon converting properties in view of photovoltaic applications: the cases of rare earth-doped zinc oxide and cerium oxide. *Université de Strasbourg*, 2014.

[46] Tao, Y., De Luca, O., Sing, B., Kamphuis, A.J., Chen, J., Rudolf, P., and Pescarmona, P.P. WO_3-SiO_2 nanomaterials synthesized using a novel template-free method in supercritical CO_2 as heterogeneous catalysts for epoxidation with H_2O_2. *Materials Today Chemistry*, 18, 2020.

[47] Tran, H.H., Truong, D.H., Truong, T.T., Nguyen, T.X.D., Jin, Y.S., Kim, S.J., and Vo, V. A Facile Synthesis of WS2/g-C3N4Composites with Improved Photocatalytic Activity. *Bull. Korean Chem. Soc.*, 39:965–971, 2018.

[48] Sarma, D.D. and Rao, C.N.R. XPES Studies of Oxides of Second= and Third-Row Transition Metal including Rare Earths. *Journal of Electron Spectroscopy and Related Phenomena*, 20:25–45, 1980.

[49] Simchi, H., Choudhury, T.H., Walter, T.N., and Kirkley, L.Y. Sulfidation of 2D Transition Metals (Mo, W, Re, Nb, Ta): Thermodynamics, Processing, and Characterization. *Journal of Materials Science*, 52:10127–10139, 2017.

[50] Izawa, K., Ida, S., Unal, U., and Yamaguchi, T. A new approach for the synthesis of layered niobium sulfide and restacking route of NbS. *Journal of Solid State Chemistry*, 181:319–324, 2008.

[51] Ballantini, R., Daccà, A., Gemme, G., and Parodi, R. Improvement of the Maximum Field of Accelerating Cavities by Dry Oxidation. *INFN Sezione di Genova*, 2014.

[52] Ettema, A.R.H.F. and Haas, C. An X-ray photoemission spectroscopy study of interlayer charge transfer in some misfit layer compounds. *J. Phys.: Condens. Matter*, 5:3817, 1993.

[53] Kwoka, M., Galstyan, V, Comini, E., and Szuber, J. Pure and Highly Nb-Doped Titanium Dioxide Nanotubular Arrays: Characterization of Local Surface Properties. *Nanomaterials*, 7:456, 2017.

[54] Loh,L., Zhang, Z., Bosman, M., and Eda, G. Substitutional doping in 2D transition metal dichalcogenides. *Nano Research*, 14:1668–1681, 2020.

[55] Yan, R., Khalsa, G., Schaefer, B.T., Jarjour, A., Rouvimov, S., Nowack, K.C., Xing, H.G., and Jena, D. Thickness dependence of superconductivity in ultrathin NbS_2. *Appl. Phys. Express*, 12, 2019.

[56] Kozhakhmetov, A. CVD Growth And Characterization of 2D NbS_2. Master's thesis, Pennsylvania State University, 2017.

[57] Lan, C.Y., Li, C., Ho, J.C., and Liu, Y. 2D WS_2: From Vapor Phase Synthesis to Device Applications. *Adv. Electron. Mater.*, 7, 2021.

[58] Hossain, N., Günes, O., Zhang, C., Koughia, C., Li, Y., Wen, S.J., Wong, R., Kasap, S., and Yang, Q. Structural and physical properties of NbO_2 and Nb_2O_5 thin flms prepared by magnetron sputtering. *J Mater Sci: Mater Electron*, 30:9822–9835, 2019.

[59] Luth H. *Solid Surfaces, Interfaces and Thin Films*. Springer, 2001.

[60] Naito, M. and Tanaka, S. Electrical Transport Properties in $2H$-NbS_2, -$NbSe_2$, -TaS_2 and -$TaSe_2$. *Journal of the Physical Society of Japan*, 51:219–227, 1982.

[61] Niazi, A. and Rastogi, A.K. Low-temperature resistance minimum in non-superconducting $3R$-$Nb_{1+x}S_2$ and $3R$-Ga_xNbS_2. *J. Phys.: Condens. Matter*, 13:6787, 2001.

[62] Anantharaj, S., Ede, S.R., and Karthick, K. Precision and correctness in the evaluation of electrocatalytic water splitting: revisiting activity parameters with a critical assessment. *Energy Environ. Sci.*, 11:744, 2018.

[63] Houssa, M., Dimoulas, A., and Molle, A. *2D Materials for Nanoelectronics*. CRC Press, 2016.

[64] Shang, X., Tang, J.H., Dong, B., and Sun, Y.J. Recent advances of nonprecious and bifunctional electrocatalysts for overall water splitting. *Sustainable Energy Fuels*, 4:3211, 2020.

[65] Shiraz, H.G., Crispin, X., and Berggren, M. Transition metal sulfides for electrochemical hydrogen evolution. *International Journal of Hydrogen Energy*, 46:24060–24077, 2021.

[66] Campos-Roldán. C.A. and Alonso-Vante, N. The Hydrogen Evolution Reaction on Nanostructured Molybdenum Disulfide. *J. Mex. Chem. Soc.*, 63:3, 2018.

[67] Wang, J., Liu, J. abd Zhang, B. abd Ji, X. Xu, K., Chen, C. andMiao, L., and Jiang, J. The mechanism of hydrogen adsorption on transition metal dichalcogenides as hydrogen evolution reaction catalyst. *Phys. Chem. Chem. Phys*, 19:10125–10132, 2017.

[68] Shin, S., Jin, Z., Kwon, D.H., Bose, R., and Min, Y.S. High Turnover Frequency of Hydrogen Evolution Reaction on Amorphous MoS_2 Thin Film Directly Grown by Atomic Layer Deposition. *Langmuir*, 31:1196–1202, 2015.

[69] Lei, Y., Pakhira, S., Fujisawa, K., and Wang, X. Low-temperature Synthesis of Heterostructures of Transition Metal Dichalcogenide Alloys ($W_xMo_{1x}S_2$) and Graphene with Superior Catalytic Performance for Hydrogen Evolution. *ACS Nano*, 11:5103–5112, 2017.

[70] Najafi, L., Bellani, S., Oropesa-Nuñez, R., Martín-García, B., Prato, M., Mazánek, V., Debellis, D., Lauciello, S., Brescia, R., Sofer, Z., and Bonaccorso, F. Niobium disulphide (NbS_2)-based (heterogeneous) electrocatalysts for an efficient hydrogen evolution reaction†. *Journal of Materials Chemistry A*, 7:25593–25608, 2019.

[71] Forrister, T. Analyzing Cyclic Voltammetry at a Microdisk Electrode with Simulation, 2018.

[72] Dupont, M., Hollenkamp, A.F., and Donne, S.W. Electrochemically active surface area effects on the performance of manganese dioxide for electrochemical capacitor applications. *Electrochimica Acta*, 104:140–147, 2013.

[73] McCrory, C.C.L., Jung, S., Ferrer, I.M., Chatman, S.M., Peters, J.C., and Jaramillo, T.F. Benchmarking Hydrogen Evolving Reaction and Oxygen Evolving Reaction Electrocatalysts for Solar Water Splitting Devices. *Journal of the American Chemical Society*, 13:4347–4357, 2015.

[74] Wu, L., van Hoof, A.J.F., Dzade, N.Y., Gao, L., Richard, M.I., Friedrich, H., De Leeuw, N.H., Hensen, E.J.M., and Hofmann, J.P. Enhancing the electrocatalytic activity of 2H-WS_2 for hydrogen evolution via defect engineering. *Phys. Chem. Chem. Phys.*, 21:6071, 2019.

[75] Yang, J., Mohmad, A.R., Wang, Y., Fullon, R., Song, X., Zhao, F., Bozkurt, I., Augustin, M., Santos, E.J.G., Shin, H.S., Zhang, W., Voiry, D., Jeong, H.Y., and Chhowalla, M. Ultrahigh-current-density niobium disulfide catalysts for hydrogen evolution. *Nat. Mat.*, 18:1309–1314, 2019.

[76] Zhang, W.X., Huang, Z.S., Zhang, W.L., and Li, Y.R. Two-dimensional semiconductors with possible high room temperature mobility. *Nano Research*, 7:1731–1737, 2014.

[77] Liu. M.M., Wei, S., Shahi, S., Jaiswal, H.N., Paletti, P., Fathipour, S., Remškar, M., Jiao, J., Hwang, W., Yao, F., and Li, H. Enhanced carrier transport by transition metal doping in WS_2 field effect transistors. *Nanoscale*, 12:17253–17264, 2020.

[78] Suh J., Park, T.E., Lin, D.Y., Fu, D., Park, J., Jung, H.J., Chen, Y., Ko, C., Jang, C., Sun, Y., Sinclair, R., Chang, J., Tongay, S., and Wu, J. Doping against the Native Propensity of MoS_2: Degenerate Hole Doping by Cation Substitution. *Nano Lett.*, 14:6976–6982, 2014.

[79] Nasrollahzadeh, M., Atarod, M., Sajjadi, M., Sajadi, M., and Issaabadi, Z. Plant-Mediated Green Synthesis of Nanostructures: Mechanisms, Characterization, and Applications. *Interface Science and Technology*, 28:199–322, 2019.

[80] Anantharaj, S., Karthik, P.E., and Noda, S. The Significance of Properly Reporting Turnover Frequency in Electrocatalysis Research. *Angew. Chem. Int. Ed.*, 60:23051–23067, 2021.

[81] Reggente, M., Passeri, D., and Rossi, M. Electrochemical atomic force microscopy: In situ monitoring of electrochemical processes. *AIP Conference Proceedings*, 1873:020009, 2017.

[82] Yagati, A.K., Min, J., and Choi, J.W. *Electrochemical Scanning Tunneling Microscopy (ECSTM) – From Theory to Future Applications.* Modern Electrochemical Methods in Nano, Surface and Corrosion Science, 2013. Chapter 3.

Appendix A

Electrical properties

A.1 Oxidation effects on the electrical properties

Details on the effect of oxidation of the films on the electrical properties are presented in this section. Three $Nb_xW_{1-x}S_2$ films were created with a cycle ratio of [1:3] and stored for approximately two months, each under a different condition: ambient air, in a glovebox with constant water and oxygen levels (< 0.1 ppm) and in a desiccator to prevent exposure to air.
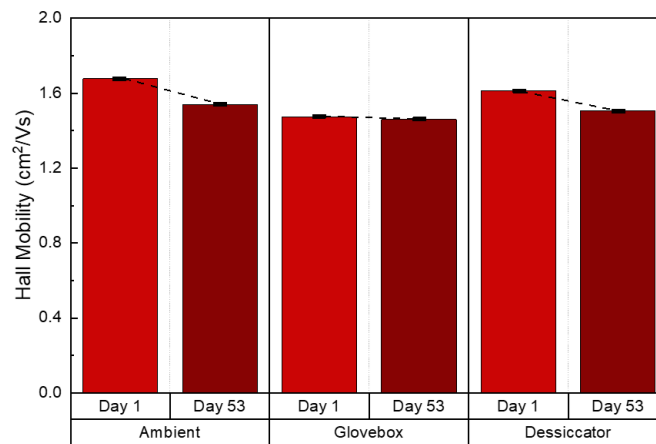
Figure A.1: Measurements of the Hall mobility μ_H measured for three $Nb_xW_{1-x}S_2$ films kept at three different conditions on the first day and approximately two months after fabrication.
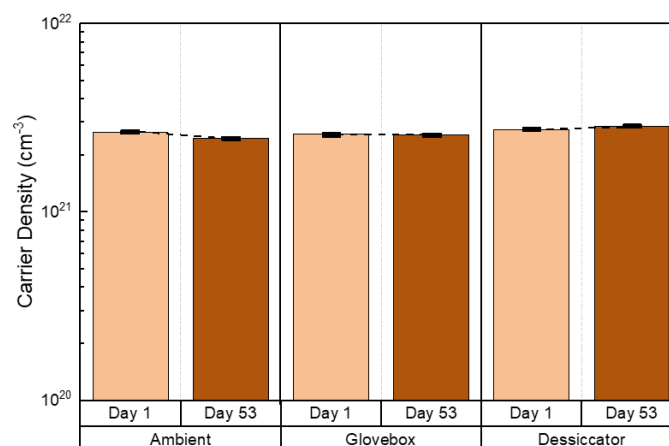
Figure A.2: Measurements of the carrier density n for three $Nb_xW_{1-x}S_2$ films each kept at different conditions, on the first day and approximately two months after fabrication.
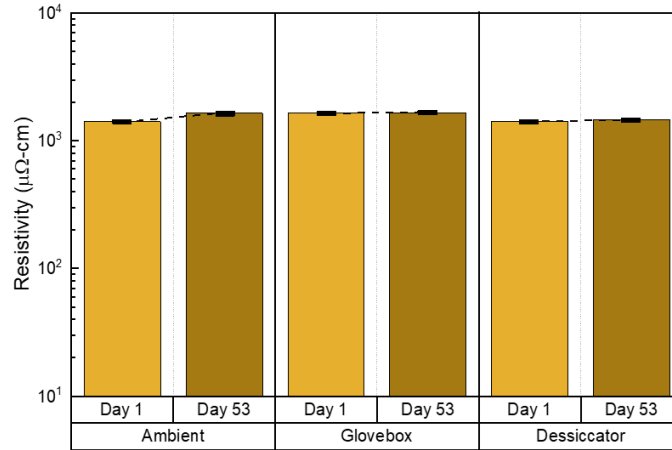
Figure A.3: Measurements of the resistivity ρ for three $Nb_xW_{1-x}S_2$ films kept at three different conditions on the first day and approximately two months after fabrication.

A.1.1 XPS depth profiling

XPS depth profiling is performed to assess the oxidation at the surface for the following three conditions: in ambient air, in a glovebox and in desiccator. An ion gun of 1000 eV is used with an estimated etch rate of 0.21 nm/sec. An etch cycle of 10 s was performed three times, which means that approximately 6 nm of the film was etched. The highest intensity of the O 1s peak is observed for the film stored under ambient conditions, while the lowest intensity is found for the film stored in the glovebox. The presence of the peaks for the Nb^{5+} and W^{6+} oxidation states disclose that Nb_2O_5 and WO_3 are formed at the surface when stored under ambient conditions. For the storage in the glovebox or desiccator, these peaks are hardly visible in the XPS spectra. It shows that the degradation in the electrical performance can be contributed to the formation of an oxide layer.
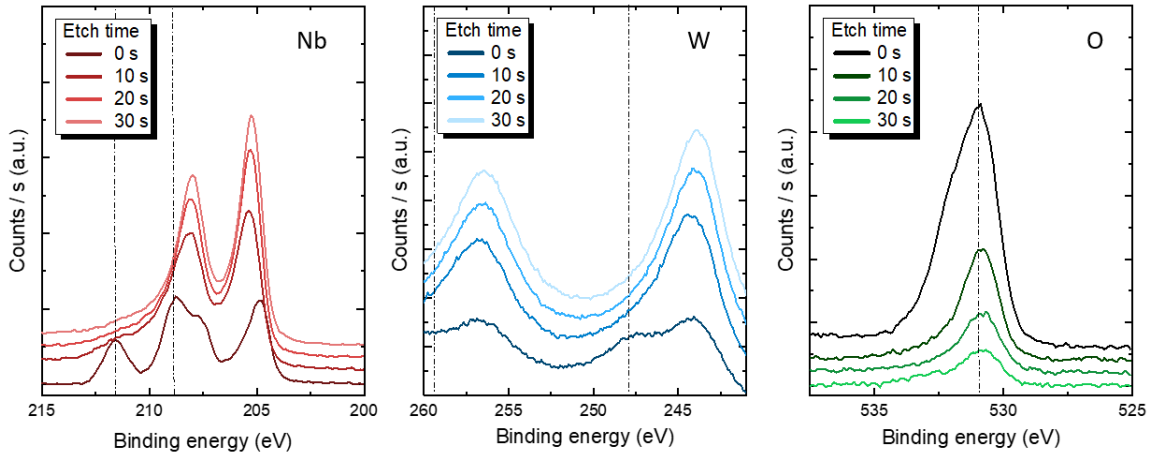
Figure A.4: Depth profiling of the [1:3] film under ambient conditions. The dashed line indicating the presence of Nb^{5+}, W^{6+}, and O^{2-} peaks corresponding to Nb_2O_5 and WO_3. The intensity of the peaks decrease after every single etch of 10 s.
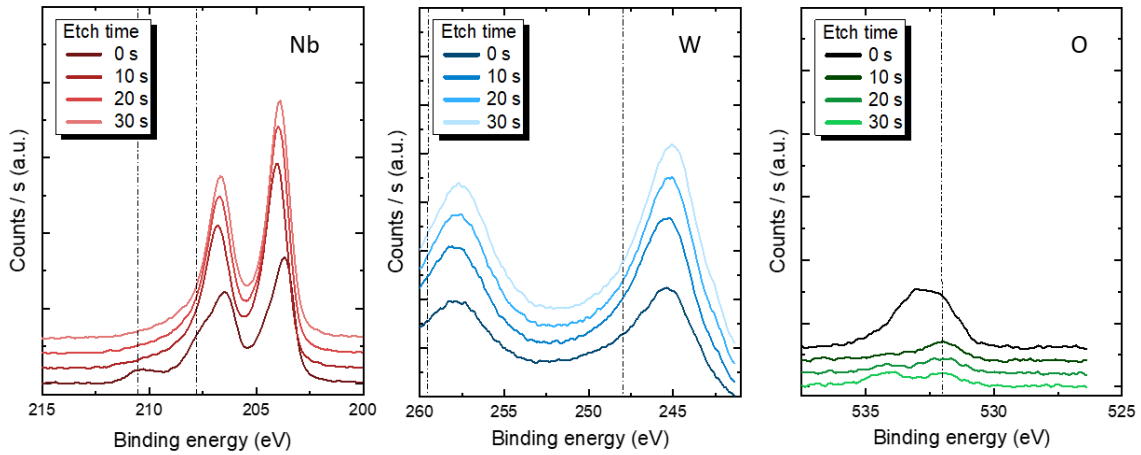
Figure A.5: Depth profiling of the [1:3] film under conditions stored in a glovebox. The dashed line indicates the presence of Nb^{5+}, W^{6+}, and O^{2-} peaks corresponding to Nb_2O_5 and WO_3.
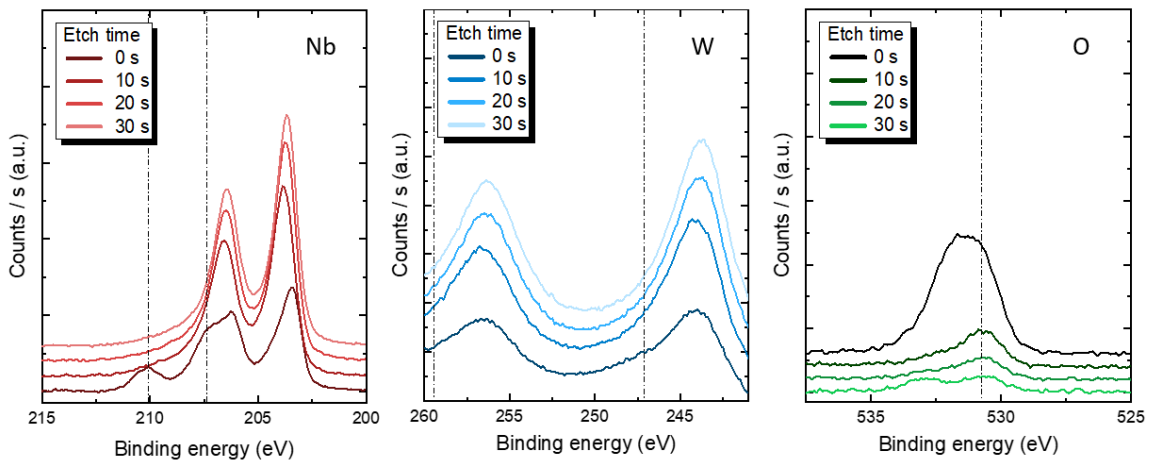

Figure A.6: Depth profiling of the [1:3] film stored in a desiccator. The dashed line indicates the presence of Nb^{5+}, W^{6+}, and O^{2-} peaks corresponding to Nb_2O_5 and WO_3. Increasing the etch time results in a significant decrease in the O 1s peak.

A.2 Temperature-dependent resistivity measurements

The temperature-dependent resistivity measurements are performed using an Ecopia HMS-5300 Hall Effect Measurement System with a temperature ranging between 120 and 297 K. The results of these measurements are presented in Figure A.7. Moreover, the carrier density and the Hall mobility were measured as a function of the temperature.
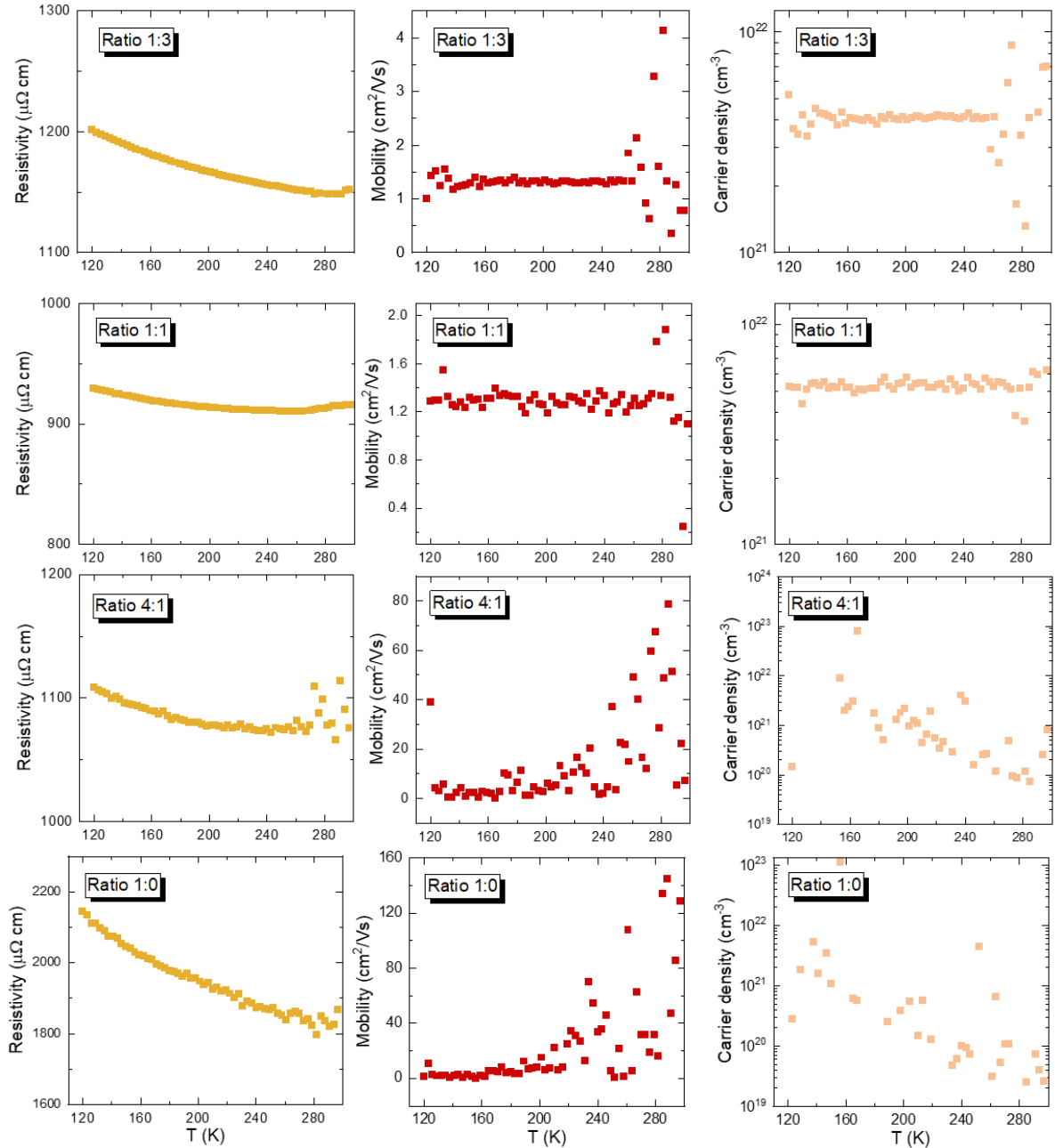
Figure A.7: Temperature-dependent resistivity measurements in the range between 120 and 300 K for cycle ratios of [1:3], [1:1], [4:1] and [1:0]. All the films show a decreasing behavior in the resistivity as a function of temperature.

Appendix B

XPS composition analysis of the HER samples
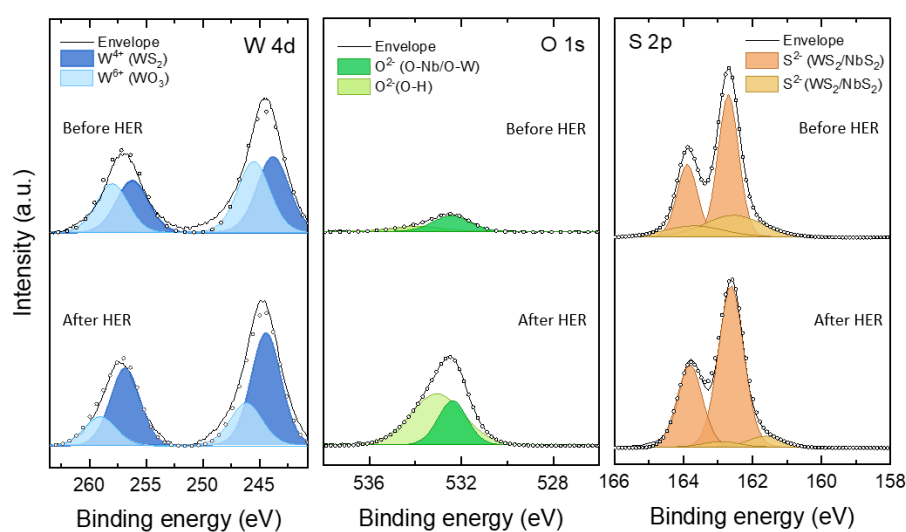
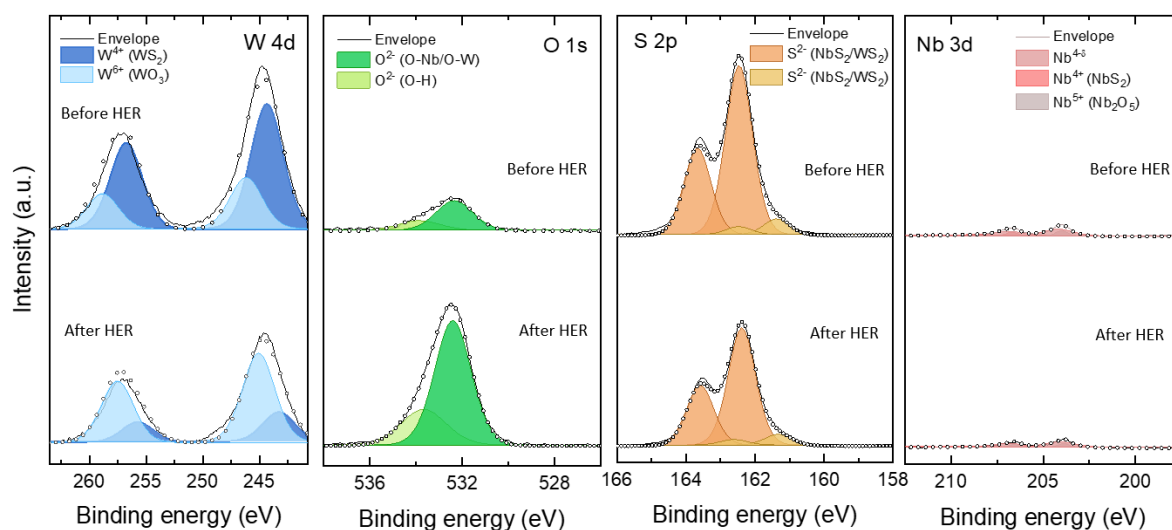**Figure B.1:** XPS composition analysis before and after the HER experiment for WS$_2$ [0:1].

Figure B.2: XPS composition analysis before and after the HER experiment for a cycle ratio [1:50].
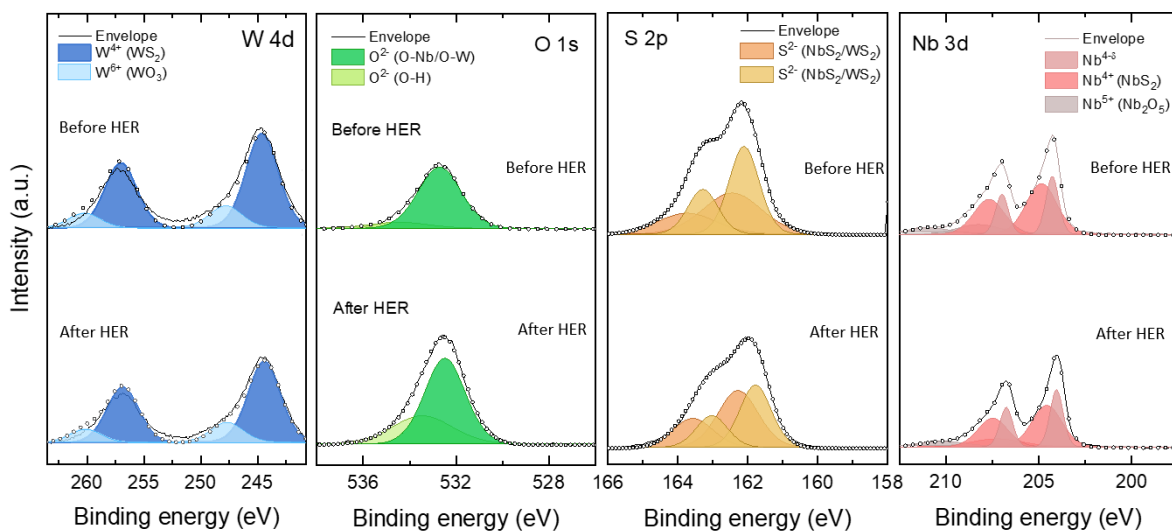
Figure B.3: XPS composition analysis before and after the HER experiment for a cycle ratio [1:3].
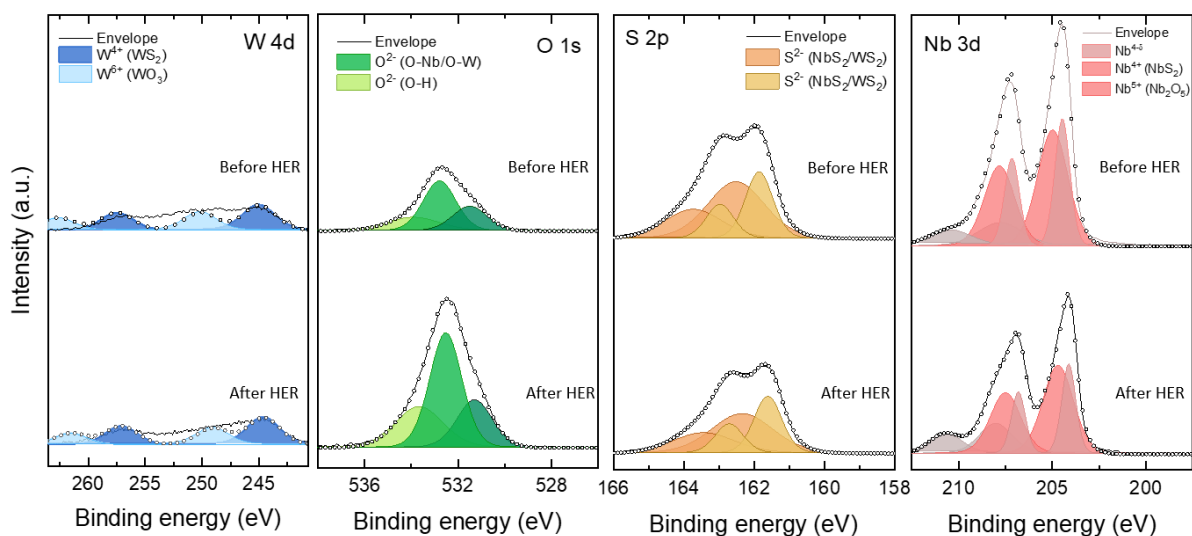

Figure B.4: XPS composition analysis before and after the HER experiment for a cycle ratio [4:1]. The graph of the W 4d scan shows a poor fit due to a very low signal-to-noise ratio.
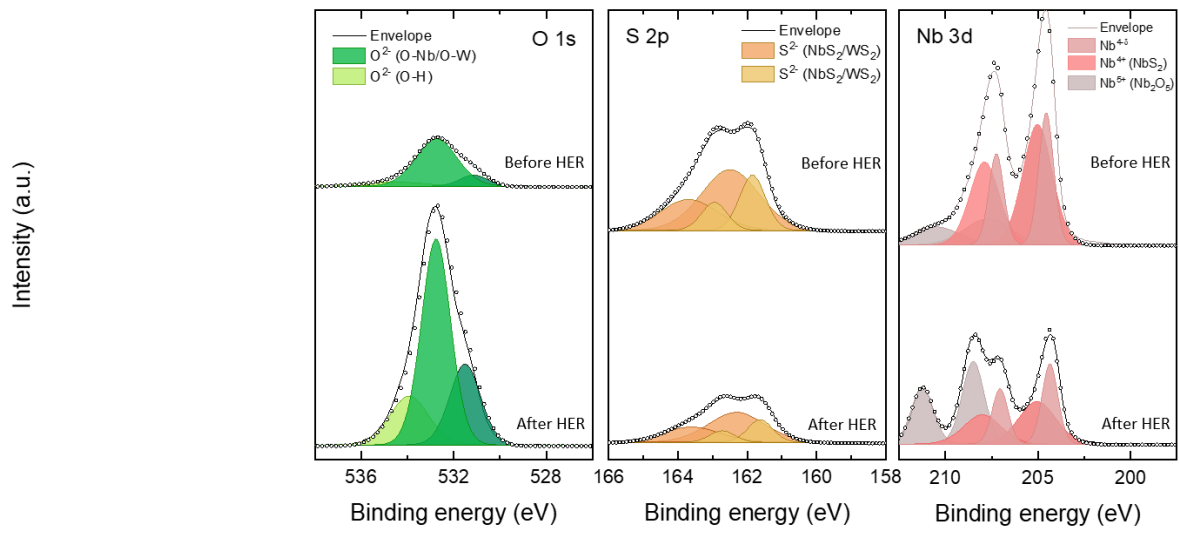
Figure B.5: XPS composition analysis before and after the HER experiment for NbS$_2$ [1:0].